AIAA JOURNAL
Vol. 52, No. 8, August 2014

Simulation of Subsonic Turbulent Nozzle Jet Flow and Its Near-Field Sound

Stefan Bühler* and Leonhard Kleiser†
ETH Zurich, 8092 Zurich, Switzerland
and
Christophe Bogey‡
École Centrale de Lyon, University of Lyon, 69134 Ecully, France

DOI: 10.2514/1.J052673

A direct numerical simulation framework is developed and validated for investigating a jet-flow configuration in which a short cylindrical nozzle and the acoustic near field are included in the simulation domain. The nozzle flow is modeled by a potential flow core and a developing turbulent wall boundary layer, which is numerically resolved. The setup allows to create well-controlled physical nozzle-exit flow conditions and to examine their impact on near-nozzle flow dynamics, jet-flow development, and the near-field sound. Turbulence at the nozzle inflow is generated by the synthetic-eddy method using flat-plate boundary-layer direct numerical simulation data and imposed softly in a sponge layer. The jet Mach number in the present investigation is $Ma = 0.9$, the diameter-based jet Reynolds number is $Re_D = 18{,}100$, and the maximum axial rms fluctuations attain 13% at the nozzle exit. The accuracy of the numerical results is checked by varying grid resolution and computational domain size. The rapid flow development in the changeover region from wall turbulence to the turbulent free shear layer within about one nozzle diameter is documented in detail. Near-field sound pressure levels compare favorably with experimental reference data obtained at the much higher Reynolds number of 780,000. This agreement is essentially attributed to a compensation of the effects of Reynolds number and turbulence level on the noise for which an empirical scaling is derived from published data. A brief comparison is also made to the jet sound field arising from a laminar nozzle-exit boundary layer.

Nomenclature

a_{ij}, T_1, T_2	=	transformation matrices
a_i, b_i, c	=	mapping function coefficients
c_f	=	skin friction coefficient
E	=	total energy
$\boldsymbol{e}_{r\theta z}, \boldsymbol{e}_{xyz}$	=	unit vectors
H	=	shape factor
L_d	=	development length
L_p, h	=	pipe (nozzle) length, thickness
L_r, L_z	=	radial, axial domain extent
Ma	=	Mach number
N	=	number of grid points
N_e	=	number of eddies
n	=	filter stencil width
P	=	number of processors
p	=	pressure
q	=	heat flux
R, D	=	nozzle radius, diameter
R_{ij}	=	Reynolds stress tensor
$Re_D = \frac{w^\diamond_{cl} \cdot \rho^\diamond_{cl} \cdot D^\diamond}{\mu^\diamond_{cl}}$	=	Reynolds number
$r_{1/2}$	=	jet half-width
$\tilde{r}$	=	auxiliary variable
(r, θ, z)	=	cylindrical coordinates
$St_D = \frac{f^\diamond D^\diamond}{w^\diamond_{cl}}$	=	Strouhal number
T_{sim}	=	simulation time
t	=	time
$\boldsymbol{U}$	=	vector of conservative variables
u_τ	=	friction velocity
$\mathbf{u}^c = (u^c, v^c, w^c)$	=	Cartesian velocities
$\mathbf{u} = (u, v, w)$	=	radial, azimuthal, axial velocity
y^+	=	normal distance to nozzle wall
z_c	=	length of potential core
$\mathbf{x} = (x, y, z)$	=	Cartesian coordinates
$\Delta r, \Delta\theta, \Delta z$	=	grid spacings
ΔT	=	time interval
Δt	=	simulation time step
δ	=	99% boundary-layer thickness
δ^*	=	boundary-layer displacement thickness
δ_ω	=	vorticity thickness
δ_Θ	=	shear-layer momentum thickness
δ_{ij}	=	Kronecker delta
$\tilde{\zeta}, \zeta_{aux}$	=	auxiliary variables
$\tilde{\zeta}_i$	=	mapping function coefficient
$\lambda_k = 2\pi/k$	=	wavelength of mode k
μ	=	dynamic viscosity
ν	=	kinematic viscosity
ρ	=	density
τ	=	viscous stress
Θ	=	boundary-layer momentum thickness
φ	=	polar angle (acoustic spectra)
$\Omega, \partial\Omega$	=	simulation domain, boundary
ω	=	wave number, circular frequency
(ξ, η, ζ)	=	computational coordinates
$\langle\cdot\rangle = \langle\cdot\rangle_{t,\theta}$	=	temporal and azimuthal average
$\langle\cdot\rangle_{t,[z_0,z_1]}$	=	temporal and axial average over $z_0 \leq z \leq z_1$

Subscripts

cl	=	centerline quantity
n	=	nozzle

Presented as Paper 2011-2921 at the 17th AIAA/CEAS Aeroacoustics Conference, Portland, OR, 6–8 June 2011; received 12 March 2013; revision received 12 August 2013; accepted for publication 19 August 2013; published online 31 January 2014.

*Research Assistant, Institute of Fluid Dynamics; buehler@ifd.mavt.ethz.ch (Corresponding Author).

†Professor, Institute of Fluid Dynamics; kleiser@ifd.mavt.ethz.ch. Member AIAA.

‡CNRS Research Scientist, Laboratoire de Mécanique des Fluides et d'Acoustique, UMR CNRS 5509; christophe.bogey@ec-lyon.fr. Member AIAA.

w	=	wall
$1/2$	=	half-width
∞	=	ambient conditions

Superscripts

$\prime\prime$	=	Favre fluctuation quantity
$+$	=	quantity in wall units
$\star$	=	coordinates for acoustic spectra
$\diamond$	=	dimensional quantity

I. Introduction

NOISE generation and radiation from compressible jet flows is a subject of high current interest. Although noise production by jet engines has been successfully reduced by introducing high-bypass-ratio turbofans, jet engines still contribute strongly to the overall aircraft noise during takeoff. As the trend of increasing bypass ratios has reached a technical upper limit, more subtle modifications of the jet flow are needed to make further progress with noise reduction. To make such modifications efficient, there is currently an enlarged research interest in basic noise-generation mechanisms, which are still not fully understood [1–3]. With the tremendous growth of computing power over the past years, numerical simulations of jet flows have become feasible and can now provide useful insights. The goal of our research project was to establish a setup for numerical simulations of nozzle jet-flow configurations including the near-field sound and to employ it for an assessment of the impact of nozzle-exit flow conditions. Of particular interest in the present contribution is an investigation of the jet-flow development and noise for turbulent nozzle boundary-layer conditions with a potential flow core.

Substantial progress has been made within the past decade with the numerical prediction of noise originating from single-stream free turbulent jets, without inclusion of nozzle walls, for various inflow conditions. A direct numerical simulation (DNS) study was performed by Freund [4] at a rather low Reynolds number of $Re_D = 3600$. With large-eddy simulation (LES) techniques, jet-flow studies at Reynolds numbers up to $Re_D = 270,000$ were possible, including an evaluation of the generated noise [5–10]. A review on the status of jet noise predictions using LES is given in [11]. As pointed out in [3,11], inflow boundary conditions are crucial for the jet-flow development, and different modes of their imposition have been applied in the literature. Mostly transition to turbulence in the jet shear layer is triggered for a prescribed laminar inflow profile. A vortex-ring method was introduced in [12], whereas linear stability theory was used to trigger the most unstable modes in [10,13,14]. In the latter references, the influence of amplitudes and spectral content of linear instability modes on the jet-flow development was extensively studied.

To investigate jet flows with well-controlled nozzle-exit conditions and to get closer to conditions found in experiments, it is necessary to include the jet nozzle itself in the simulation domain. This allows to study the effects of laminar, transitional, or turbulent flow conditions on jet-flow development and radiated noise [9]. Currently, there is a strong interest in this type of nozzle jet-flow simulations because turbulence present in the initial jet shear layer can significantly influence the overall jet noise generation [15–20]. The recent work [21] has investigated effects of the initial turbulence level on the jet-flow development and sound field at $Re_D = 10^5$ and has clearly shown a strong influence. A vortex-ring tripping procedure [16] was used to disturb a Blasius-type nozzle-exit boundary layer in a pipe nozzle of one diameter length. Jet simulations with a fully turbulent pipe flow at $Re_D \approx 7500$ developing in a nozzle of 25 diameters of length have been conducted in [19,20]. In this work, a maximum axial fluctuation level of $\langle w''^2\rangle^{1/2}_{\max} \approx 18\%$ near the nozzle walls and $\langle w''^2\rangle^{1/2} \approx 5\%$ in the core region were attained at the nozzle exit.

In the present work, the nozzle flowfield is modeled as a developing pipe flow in a cylindrical nozzle of only 2.5 diameters in length with a potential flow core and a growing turbulent wall boundary layer (TBL). This allows us to study the jet-flow development initiated by the changeover from the turbulent nozzle boundary layer to the turbulent free shear layer, rather than proceeding through laminar–turbulent transition occurring only further downstream in the jet shear layer as in the previous work [10] of our group. To our best knowledge, this is the first nozzle jet-flow simulation with direct noise computation in which near-wall turbulence in the nozzle is resolved while maintaining a potential jet-flow core. In follow-up work [22], we address a detailed comparison of the impact of laminar, transitional, and turbulent nozzle boundary layers on jet-flow development and near-field noise. A few of the results for laminar nozzle-exit conditions are included herein for comparison.

The numerical simulation framework developed in our work is based on high-order numerical schemes that were already applied successfully in jet-flow simulations without nozzle [9,10,23,24]. A new parallel implementation of the schemes allows their efficient usage on massively parallel computing architectures. The well-established synthetic-eddy method (SEM) [25–27] is used to generate turbulent inflow data reproducing mean flow and turbulence statistics of a turbulent flat-plate boundary-layer DNS. Special attention was paid to an appropriate inflow-boundary treatment that minimizes the generation of artificial disturbances, which could disturb the physically generated noise. Resolution requirements of wall turbulence and available computational resources restrict the simulations to a moderate jet Reynolds number, which is chosen as $Re_D = 18,100$. This is significantly lower than Reynolds numbers of typical jet-engine exhaust flows (where Re is of the order of 10^7 [28]) but similar to recent computational studies: $Re_D = 18,100$ [29], $Re_D = 7500$ [20], and $Re_D = 3600$ [4]. The jet Mach number is $Ma = 0.9$. The sensitivity of our results to different grid resolutions and the computational domain size has been studied extensively and is also documented partially in the present paper.

The paper is organized as follows. In Sec. II, the governing equations and the employed numerical methods are summarized. The simulation setup is described with details on the coordinate mapping used to construct suitable grids and on the generation of inflow turbulence. Instantaneous and statistical flow data are presented and discussed in Sec. III for the flowfield developing inside the nozzle, the wall/free-shear turbulence changeover region, and the jet flowfield. Near-field acoustic spectra in different radiation directions are evaluated and compared to experimental data at a much higher Reynolds number. For this purpose, we make use of an empirical relation describing the influence of Reynolds number and turbulence level, which we derive from published simulation data. A brief comparison is made also to the case of a laminar nozzle boundary layer. The work is summarized and conclusions are drawn in Sec. IV.

II. Numerical Model

In the following sections, we present the basic physical modeling and some details on the applied numerical schemes, the computational setup, and boundary conditions. A full documentation is given in [9,24,30].

A. Governing Equations and Numerical Discretization

The governing equations are the compressible Navier–Stokes equations for the conservative variables $\mathbf{U} = (\rho, \rho u^c, \rho v^c, \rho w^c, E)$ solved by applying a generalized transformation [31]. The molecular viscosity μ is obtained using Sutherland's law [24]. The length scales are nondimensionalized by the nozzle radius $R^\diamond$, while the reference location for other physical quantities is chosen at the centerline of the inflow plane (point P_{cl} in Fig. 1). The reference velocity thus is the axial centerline velocity $w^\diamond_{\mathrm{cl}}$ at P_{cl}. Within the nozzle, a turbulent boundary layer develops at the inner nozzle wall while a potential flow is present in the core.

Time integration is performed by a six-step Runge–Kutta scheme of fourth-order accuracy [32]. Differentiation of convective and dissipative terms in the axial z and radial r directions is done using a central compact finite-difference scheme of 10th order [33], whereas a Fourier pseudospectral method [34] is applied in the homogeneous

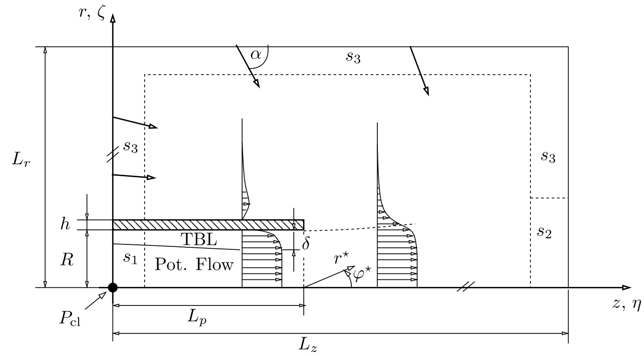

Fig. 1 Sketch of nozzle jet-flow configuration with computational domain Ω of extent $L_r \times L_z$. In regions s_1, s_2, and s_3 the inflow, outflow, and ambient sponges are active, respectively. Sketch not to scale.

azimuthal direction θ. The order of the compact schemes is reduced gradually toward the boundary $\partial\Omega$ of the simulation domain from 10th to sixth, fifth, and third-order accuracy (see [24] for the dispersion properties of the schemes). At the inner, outer, and downstream nozzle walls $\partial\Omega_n$, no-slip Dirichlet boundary conditions are applied, and the surface temperature $T|_{\partial\Omega_n} = T_w$ is prescribed. The axis singularity is treated using the method described in [35]. The number of retained Fourier modes is linearly reduced toward the centerline to circumvent the severe time-step limitation arising otherwise [35]. The computation is stabilized by applying a mild low-pass filter to the highest wave numbers $k \geqslant 2N_\theta/3$ of the solution every second time step as in the previous work [24] (if such a simulation is underresolved, it may also be considered as a large-eddy simulation). Filtering is necessary due to the use of centered low-dissipation schemes. The corresponding filter transfer function $\hat{Q}_5\hat{G}$, derived in [36] based on approximate deconvolution, acts only on the wave numbers that are not accurately resolved by the finite-difference scheme. No additional damping [37] at nozzle edge points was found to be necessary. In the DNS of Sandberg [20], filtering to avoid grid-point-to-grid-point oscillations was required as well. The implementation of our numerical scheme has been thoroughly tested previously [23,24]. Parallelization of the overall numerical scheme is achieved by applying a global data-transposition approach [30,38].

B. Coordinate Mapping

A mapping is introduced that relates the Cartesian coordinates (x, y, z) first to the cylindrical coordinates (r, θ, z) and then to the computational space coordinates (ξ, η, ζ). Mapping functions are employed to construct suitable nonequidistant grids in the radial and axial directions. Specific properties have to be fulfilled by the mapping function $r(\zeta)$ relating the radial coordinate $r \in [0, L_r]$ to the corresponding equidistant computational coordinate $\zeta \in [0, 1]$. A large disparity of length scales is present in the flowfield between the fine-scaled wall turbulence in the nozzle boundary layer and the low-frequency, long-wavelength pressure waves emitted to the acoustic near field. The challenge is to find an appropriate mapping that effectively represents both length scales in our simulation domain. It should be chosen such that a radial distribution of grid points is obtained that properly resolves the turbulent boundary-layer scales within the nozzle and gets suitably coarsened toward the acoustic near field where only the propagation of sound pressure waves needs to be supported, while avoiding a costly overresolution in the core region of the jet. Such a mapping can be constructed by extending the approach of [39], which we also employ for the mapping $z(\eta)$ in the axial direction. The desired radial mapping is achieved by defining an auxiliary function $\partial\tilde{r}/\partial\tilde{\zeta}$ as

$$
\begin{aligned}
\frac{\partial\tilde{r}}{\partial\tilde{\zeta}}(\tilde{\zeta}) := c &+ b_1(1 - 1/2(\tanh(a_1(\tilde{\zeta} - \tilde{\zeta}_1)) + 1) \\
&- 1/2(\tanh(a_1(-\tilde{\zeta} - \tilde{\zeta}_1)) + 1)) \\
&+ b_2(1/2(\tanh(a_2(\tilde{\zeta} - \tilde{\zeta}_2)) + 1) \\
&+ 1/2(\tanh(a_2(-\tilde{\zeta} - \tilde{\zeta}_2)) + 1)) \\
&+ b_3(1/2(\tanh(a_3(\tilde{\zeta} - \tilde{\zeta}_3)) + 1) \\
&+ 1/2(\tanh(a_3(-\tilde{\zeta} - \tilde{\zeta}_3)) + 1))
\end{aligned} \tag{1}
$$

We then find the mapping $r(\zeta)$ by integrating Eq. (1) and rescaling such that $r(\zeta = 1) = L_r$. The parameters a_i, b_i, c, and $\tilde{\zeta}_i$ have to be chosen such that the aforementioned grid properties are fulfilled. Figure 2 shows an example of the mapping and the corresponding metric term. The auxiliary coordinate ζ_{aux} is introduced to treat the singularity according to [35] (see also [24]).

C. Simulation Setup

A computational domain of dimension $[0, L_r] \times [-5, L_z - 5] = [0, 20] \times [-5, 35]$ for simulation runs $A_1 - A_3$ and $[0, 30] \times [-5, 55]$ for simulation run B is introduced, as shown in Fig. 3 (see Table 1, also providing grid parameters). The length of the cylindrical nozzle (pipe) is chosen as $L_p = 5$ and the lip thickness as $h = 0.1$ in all simulation runs. Grid spacings obtained for the radial and axial directions are given in Fig. 4. A minimum radial grid spacing of $\Delta r = 0.01$ at the nozzle wall was chosen in all simulation runs. The axial grid spacing in simulation run A_1 applying $\Delta z = 0.053$ was refined to $\Delta z = 0.028$ in A_2 throughout the computational domain. A local refinement around the nozzle exit has been done in run A_3 reaching a minimum of $\Delta z = 0.02$. Simulation run B exhibits approximately the same spatial resolution $\Delta z = 0.051$ as A_1. Grid spacings are also summarized in Table 1. In Table 1 nozzle-exit grid spacings are measured at trailing edge $z = 0$ in wall units and compared to boundary layer DNS [40] data. Within the jet-flow field, absolute values for the grid spacings are related to integral length scales L_{11}^{θ} and L_{22}^{z} and compared to reference data [21]. For all computational grids, an axial grid stretching is introduced around five radii upstream of the outflow domain boundary. In combination with the sponge layer [41] and nonreflecting boundary conditions [42], this was efficient in preventing reflections from the outflow domain boundary as in previous work [9,10,23,24].

At the far-field boundary, nonreflecting boundary conditions [42] adapted to the curvilinear coordinates [43] are applied in combination

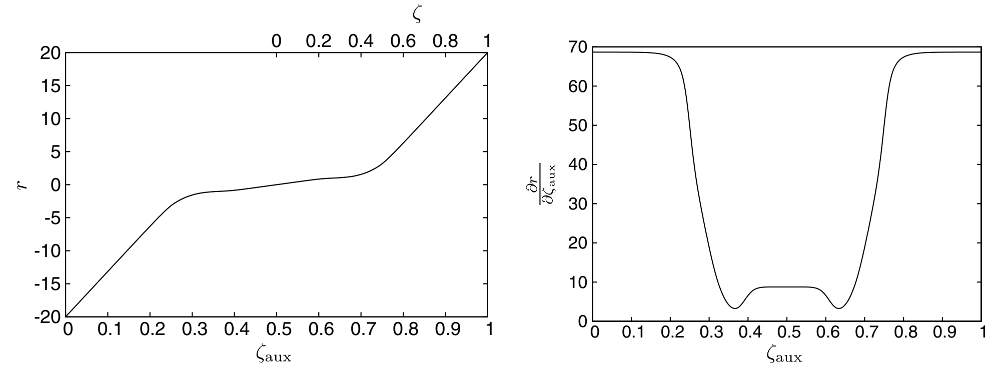

Fig. 2 Mapping $r(\zeta)$ (left) and the corresponding metric term $\partial r/\partial\zeta_{\mathrm{aux}}$ (right) for the radial direction.

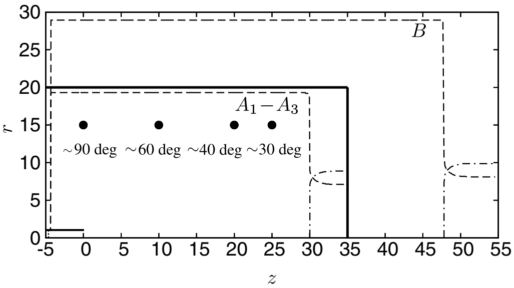

Fig. 3 Computational domains for simulation runs A_1–A_3 and B. Line types identify sponges by contour lines of $\sigma = 0.1$ for ··········· inflow, ------ ambient, and –·–·–·– outflow boundaries. Dark circles denote noise observation positions of experiment [17].

with sponge layers [41] to ensure constant mean pressure and density levels over the simulation time [44]. The ambient sponge requires special attention. The local angle α defining the direction of the mean entrainment flow (see Fig. 1) is prescribed to ensure a correct functioning of the characteristic nonreflecting boundary conditions. It is defined using the potential flow solution for the entrainment as given in generalized form by Schneider [45]. In the outflow sponge layer, the density ρ and pressure p are driven to ambient conditions to avoid drifts over the simulation time. The inflow sponge layer treatment will be discussed in more detail in Sec. II.D.

The computational time step Δt was held constant at $\Delta t = 0.002$ in simulation runs A_2 and A_3 and at $\Delta t = 0.004$ in simulation runs A_1 and B.

All simulations were run initially for at least 200 nondimensional time units, allowing transients to leave the computational domain. The simulations were then continued for another 400–600 time units, which was found sufficient to attain converged statistics. Full three-dimensional (3-D) fields were stored to disk in time steps of $\Delta T = 0.2$ to resolve nondimensional frequencies up to $St_D = 2.5$. As an example, for run A_3, approximately 5 TB of data were stored on disk.

D. Inflow Treatment for Turbulent Nozzle Boundary Layer

For the numerical simulations with a turbulent boundary layer at the inflow, three-dimensional and time-dependent inflow-boundary conditions are needed. Different techniques to generate such data are available in the literature; see [27,46]. Here, we make use of SEM, already successfully applied in previous work [47]. At the inflow to the nozzle, we prescribe a potential flow (i.e., a constant bulk velocity w) in the core region, whereas a turbulent boundary-layer profile with momentum thickness $\Theta = 0.033$ ($\delta = 0.3$) is introduced at the wall. The time-dependent inflow boundary velocity $\mathbf{u}_{\mathrm{SEM}} = \langle \mathbf{u}_{\mathrm{SEM}} \rangle + \mathbf{u}''_{\mathrm{SEM}}$ is computed by the SEM in such a way that the mean flow $\langle \mathbf{u}_{\mathrm{SEM}} \rangle$ and Reynolds-stress profiles $\langle \mathbf{u}''^2_{\mathrm{SEM}} \rangle^{1/2}$ agree with the corresponding reference incompressible, flat-plate boundary-layer simulation data [40] at $Re_\Theta = 300$. Details of the method including its adaptation to the cylindrical coordinates are given in [30]. For simplicity, the synthetic eddies induce velocity fluctuations following a tent function with constant length scale [26] of $l_{\mathrm{SEM}} = \kappa \cdot \delta = 0.12$ independent of the wall-normal distance. Following test cases presented in [26], the number of eddies is chosen as $N_e = 100$. Figure 5 shows that, as intended, the SEM is capable of generating a turbulent inflow reproducing the statistics of prescribed reference data (minor deviations are related to the mapping of synthetic fluctuations to given Reynolds-stress profiles; see [48,49]). For the extension of SEM to compressible flows, we use the strong Reynolds analogy to determine temperature fluctuations as proposed in [46,50], and the mean temperature distribution $\langle T \rangle$ is estimated using a Crocco–Busemann relation [51]. Although this relation has been derived for laminar compressible boundary layers, it is known to give a reasonable estimate also in the turbulent case [51]. The density ρ_{SEM} is then obtained from the equation of state assuming constant ambient pressure across the boundary layer and set as well. This avoids its mean drift over simulation time otherwise known to arise when applying nonreflecting boundary conditions [44,52]. The inflow sponge reference solution finally reads [30] $\mathbf{U}_{\mathrm{SEM}} = (\rho_{\mathrm{SEM}}, u^c_{i,\mathrm{SEM}}, E_t(u^c_{i,\mathrm{SEM}}, T_{\mathrm{SEM}}))^\top$.

Special care has been taken to avoid nozzle-based sound sources, as were found in [20]. For this purpose, we softly enforce the nominal turbulent inflow $\mathbf{U}_{\mathrm{SEM}}$ by a sponge-layer technique [41]:

$$\frac{\partial}{\partial t}(\mathbf{U}) = \mathcal{RHS}(\mathbf{U}) + \sigma_{\mathrm{inl}}(\mathbf{U} - \mathbf{U}_{\mathrm{SEM}}) \tag{2}$$

In combination with the nonreflecting boundary conditions, this inflow treatment is considered to prevent reflections of upstream-traveling sound waves, which could possibly disturb the flow or the acoustic near-field development. In spite of this damping, the forcing needs to be strong enough to impose turbulence effectively onto the boundary layer developing at the nozzle wall. This is achieved by varying σ_{inl} smoothly from $\sigma_{\mathrm{inl}} = 1$ at the inflow $z = -5$ toward $\sigma_{\mathrm{inl}} = 0$ at $z = -4.7$.

$Re_\Theta = 300$ corresponds to the lowest Reynolds number for which we can expect a turbulent boundary layer to exist [40]. This low value was chosen here to minimize the overall computational cost of our simulation. With the (arbitrary) choice of $\delta = 0.3R$ ($\Theta = 0.033R$), the Reynolds number Re_D is related to Re_Θ as

$$Re_D = \frac{w^\diamond_{\mathrm{cl}} \cdot \rho^\diamond_{\mathrm{cl}} \cdot \Theta^\diamond}{\mu^\diamond_{\mathrm{cl}}} \cdot \frac{D}{\Theta} = Re_\Theta \cdot \frac{D}{\Theta} = 18,100 \tag{3}$$

Table 1 Computational domain size and grid parameters

	A_1 (reference)	A_2 (refined in z)	A_3 (refined in r, θ, z)	B (larger domain)	Reference data
			Domain size		
$L_r \times L_z$	20×40	20×40	20×40	30×60	— —
			Number of points		
N_r	384	384	448	480	— —
N_θ	128	128	256	128	— —
N_z	640	1280	768	1024	— —
		Nozzle-exit flow, $z = 0$ (with reference data: DNS: TBL [40])			
Number of points in $y^+ < 10$	4	4	6	4	10
Δr^+_w	3	3	1.6	3	~1
$R^+ \Delta\theta$	15	16	8	15	7
Δz^+	17	9	6	17	20
		Jet flow (with reference data [21], $Re_D = 10^5$, $\langle w'^2 \rangle^{1/2} = 0\% \ldots 12\%$)			
Δz	0.053	0.028	0.022	0.051	0.007
$R\Delta\theta$	0.049	0.049	0.025	0.049	0.006
$L^z_{11}\vert_{\min}$	0.23	0.23	0.19	0.23	0.450 . . . 0.054
$L^\theta_{11}\vert_{\min}$	0.26	0.26	0.25	0.26	2.059 . . . 0.010
$L^z_{11}\vert_{\min}/\Delta z$	4	8	10	4	4–7
$L^\theta_{11}\vert_{\min}/R\Delta\theta$	5	5	8	5	1.6

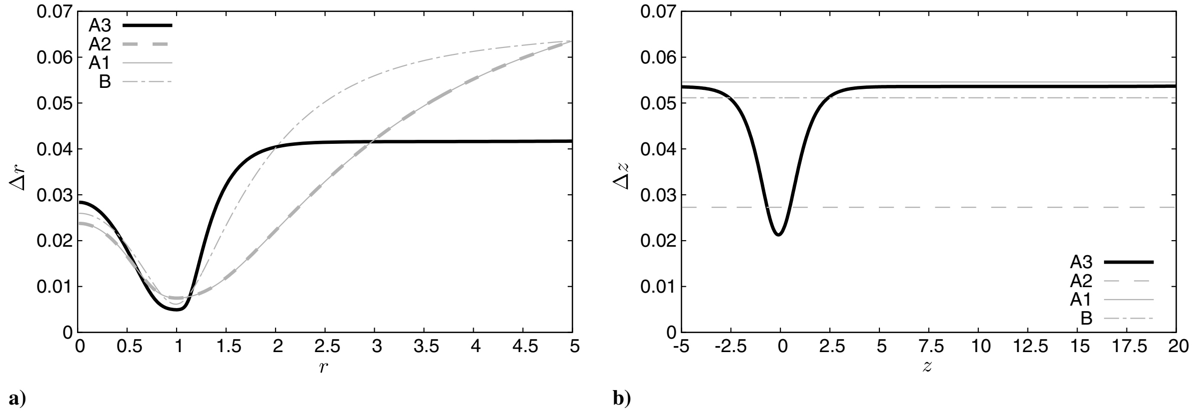

Fig. 4 Grid spacings in a) radial, and b) axial direction for the grids given in Table 1, simulation runs —— A_1, - - - - A_2, —— A_3, and -·-·- B.

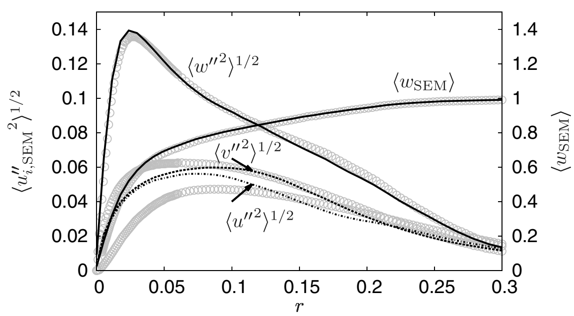

Fig. 5 Favre-averaged axial mean flow profile $\langle w_{\mathrm{SEM}}\rangle_{\theta t}$ and rms fluctuations $\langle u''^2_{i,\mathrm{SEM}}\rangle^{1/2}_{\theta t}$ generated by SEM in comparison with reference data of Spalart (open circles) [40].

A nozzle jet-flow configuration with a similar nozzle-exit momentum thickness was studied in [16]. After some streamwise development length L_d, estimated from test cases in [26] to be $L_d \approx 10\delta = 3R < L_p = 5R$, we can expect that the synthetic inflow turbulence has largely relaxed toward a turbulent state before the nozzle exit.

III. Jet Flow Arising from Turbulent Nozzle Boundary Layer

In this section, we present results of our nozzle jet-flow simulations including the direct computation of the near-field sound. We discuss the development of the turbulent boundary layer in the nozzle and its changeover to the turbulent free shear layer (Sec. III.A), the turbulent jet-flow development (Sec. III.B), and finally the sound emitted to the acoustic near field (Sec. III.C). The accuracy of the numerical results is checked by varying the grid resolution within the developing turbulent wall boundary layer and in the vicinity of the nozzle-exit plane for constant computational domain size (simulation runs A_1–A_3, cf. Table 1). For the development of the acoustic field, the computational domain size is important because it may influence low-frequency acoustic waves whose wavelength is of the same order as the domain length or width. An additional simulation run B was therefore carried out with an enlarged computational domain (cf. Table 1). In the following, we discuss the jet-flow development and near-field noise obtained in run A_3. The comparison with results of the other simulation runs (which are partially included in the figures) will be briefly discussed at the end of each section.

A. Flowfield in Nozzle and Near Trailing Edge

1. *Instantaneous Flow*

To get a first glance at the turbulent boundary layer developing in and immediately behind the nozzle, a 3-D visualization of vortical structures is given in Fig. 6. Although the jet Mach number is subsonic ($Ma = 0.9$), localized slightly supersonic regions can exist due to vortices in the jet shear layer. Streamwise-elongated vortical structures are associated with the well-known low/high-speed streaks of the turbulent nozzle boundary layer. They persist downstream only for about one nozzle diameter before they rapidly decay into smaller-scale structures. The front view illustrates the free shear layer development surrounding the potential flow core.

In addition to the near-wall streaks, we also observe the development of localized turbulent spots, which appear randomly. Figure 7a shows the 3-D visualization of a single turbulent spot with the typical development of hairpin vortices at the front tip [54]. In Fig. 7b the boundary layer thickness $\delta = 0.3R$ chosen at the inflow is indicated by the dashed line. The spots grow as they are convected downstream, but the nozzle length is too short to allow spots to merge.

This indicates that transition to fully developed turbulent flowfield has not yet been finalized within our nozzle (i.e., the boundary layer may be considered to be in a late transitional stage). Note that a nozzle of length $L_p = 50$ radii was necessary to establish a fully developed turbulent pipe flow in [20]. For the rest of this work, we refer to the boundary-layer state reached at the nozzle exit $z = 0$ as developing turbulent. Parameters are listed in Table 2 (see also the discussion in Sec. III.A.2).

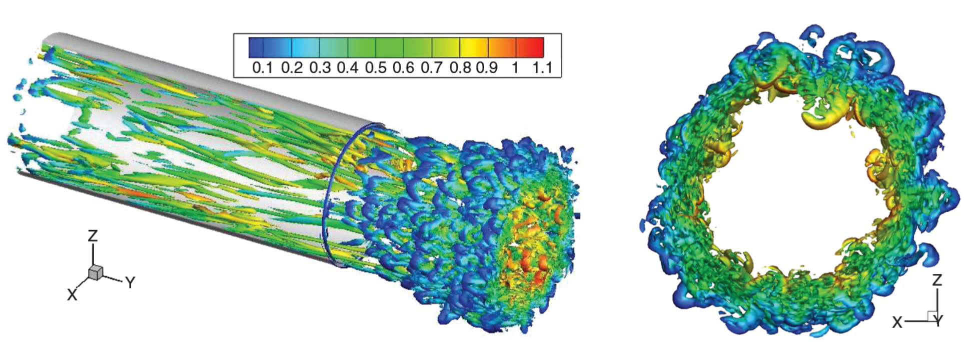

Fig. 6 Visualization of vortical structures by isosurfaces [53] $\lambda_2 = -0.8$ within the nozzle $-5 \lesssim z \lesssim 0$ and in the beginning jet shear layer $0 \lesssim z \lesssim 3$. Right panel: end view looking upstream. The color corresponds to the local Mach number.

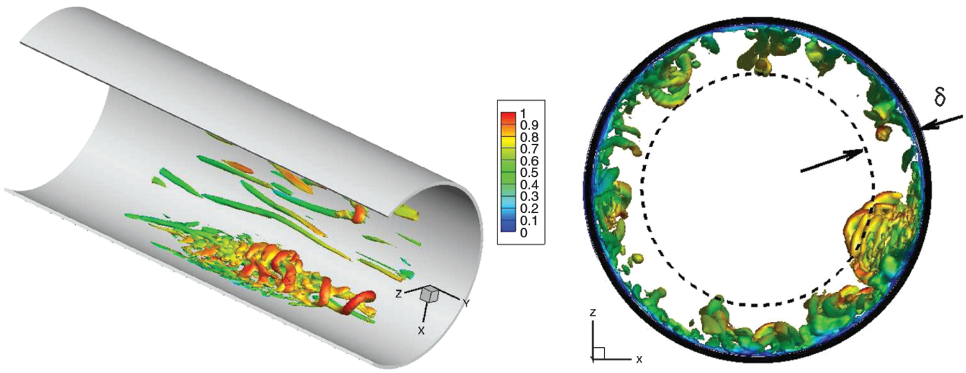

Fig. 7 Left: instantaneous isosurface $\lambda_2 = -0.6$ colored with local Mach number, illustrating localized spots in the developing turbulent boundary layer $-5 \leqslant z \leqslant 0$. Right panel: end view looking upstream.

A brief comparison will also be made with a jet flow arising from laminar nozzle-exit conditions. For this simulation (using the grid applied in run B), a laminar boundary layer of similar momentum thickness was introduced at the inflow. Nozzle-exit data are documented in Table 2 for turbulent (TU, simulation run A_3) and laminar (LA, simulation run using grid B) nozzle exit conditions. Details are also given in [22].

Figure 8 shows contours of the instantaneous azimuthal vorticity and provides an overview of the flow development, in which we identify four different regions $R_1 - R_4$: R_1 developing turbulent boundary layer ($z \leq 0$), R_2 changeover region ($0 \leq z \leq 2$), R_3 developing jet shear layer with closing of potential core at $z_c \approx 12$ and R_4 self-similar jet ($z \gtrsim 20$). Beyond the trailing edge, the developing turbulent boundary layer rapidly changes over into a turbulent jet shear layer. The potential flow core region narrows and is closed approximately $z_c = 12$ radii downstream of the nozzle exit. Further downstream (beyond $z \approx 20$), the jet-flow development becomes self-similar as will be shown next.

The development of velocity fluctuations within the four flow regions is visualized in Fig. 9. Contours of instantaneous axial velocity fluctuations are visualized on a cylindrical surface at a wall-normal distance of $y^+ \approx 8$ at the nozzle exit. Local values of $u_\tau = \sqrt{\tau_w/\rho}$ are used to compute wall units. In the turbulent nozzle boundary layer, low- and high-speed streaks with an axial extent of approximately $\Delta z^+ \approx 1000$ (three nozzle radii) are present as expected [55]. The streaks persist downstream of the nozzle exit $z = 0$ for approximately one to two radii before they rapidly decay into smaller turbulent structures, as already seen in Fig. 6. Within the further jet development, the size of the turbulent structures appears to increase linearly with z (see also Sec. III.A.3).

2. *Mean Flow and Root-Mean-Square Statistics*

To quantify the development of the turbulent nozzle boundary layer, Fig. 10 shows the skin friction measured along the inner (Fig. 10a) and outer (Fig. 10b) nozzle walls (unless stated otherwise, $\langle\cdot\rangle = \langle\cdot\rangle_{t,\theta}$ denotes averaging in the azimuthal direction and in time). The skin friction at the inner nozzle wall slightly increases toward the nozzle exit. Because of the entrainment of fluid into the developing jet shear layer, a laminar boundary layer establishes at the outer nozzle wall. There, a sharp increase of the skin friction is observed in the vicinity of the nozzle trailing edge. This increase is consistent with the analytical predictions [56] for laminar boundary layers approaching the trailing edge of a flat plate (shown in Fig. 10b by the circles). We observe no sharp increase of c_f along the inner nozzle wall for our developing turbulent boundary layer. A strong increase of c_f has been found in the simulations of [19], where, however, a fully developed turbulent pipe flow was present in the nozzle. It is worth mentioning that no strong numerical oscillations were observed within the nozzle or near the trailing edge in any of the simulation runs. This suggests sufficient resolution, because low-dissipation numerical schemes in general are likely to produce numerical oscillations when flow phenomena are underresolved [20].

Grid spacings in wall units $\Delta x_i^+ = \Delta x_i u_\tau Re_R/\nu_w$ are summarized in Table 1. The distance of the first radial grid point away from the wall is indicated by Δr_w^+. Also given is the number of grid points placed within the first 10 wall units: four points in A_1 and A_2 and six in A_3, leading to similar results. In run A_3, grid spacings are refined in all spatial directions, yielding a wall-normal and axial (streamwise) resolution (at the trailing edge) even finer than a standard boundary-layer DNS [40]. The results for the jet mean flow development discussed in the following were not significantly influenced by the grid refinements.

The mean streamwise velocity profiles $w^+ = \langle w\rangle/u_\tau$ and turbulence intensities $u_i''^+ = \langle u_i'' u_i''\rangle^{1/2}/u_\tau$ in the boundary layer are presented in Fig. 11. The obtained mean flow profiles shown in Fig. 11a are clearly different from the laminar Blasius boundary-layer profile but have not yet quite reached the fully turbulent state. The reason for the slight overprediction in the log-law region $30 \leqslant y^+ \leqslant 80$ is most probably related to the inflow boundary treatment, the rather short nozzle, and the low value of $Re_\Theta = 300$. As previously discussed in Sec. II.D, we rely on sponge (forcing) layers to impose the turbulent fluctuations at the inflow. This allows for the necessary flow adjustment, but fluctuations computed by SEM are only weakly enforced by the term added to the right-hand side [Eq. (2)] rather than being strongly enforced by Dirichlet boundary conditions. Therefore, triggering turbulence cannot be as efficient as in the test cases presented in [26], which apply Dirichlet boundary conditions. It should also be noted that some differences of our compressible boundary layer developing under a favorable pressure gradient in a circular nozzle to incompressible, zero-pressure-gradient, flat-plate boundary-layer reference data are to be expected. However, Fig. 11b shows that we have already reached a level of axial turbulent fluctuations comparable to that found in fully turbulent boundary layers ($w_{\max}''^+ = 2.5$ in [40]). For the radial and azimuthal fluctuations, rms peak levels reach $u_{\max}''^+ = 0.5$ and $v_{\max}''^+ = 0.7$, respectively, which is lower than typically found in a flat-plate turbulent boundary layer ($u_{\max}''^+ = 1.2$ and $v_{\max}''^+ = 1.5$ in [40]). This is mainly attributed to the usage of sponge layers. The downstream development of the rms profiles shows a slight shift toward the centerline, which can be associated with the displacement effect of the growing boundary

Table 2 Boundary layer data at nozzle exit plane ($z = 0$) and length of potential core

	δ^*	Θ	$H = \delta^*/\Theta$	c_f	$\langle w''^2\rangle_{\max}^{1/2}$	$\langle u''^2\rangle_{\max}^{1/2}$	$\langle v''^2\rangle_{\max}^{1/2}$	L_{pc}
TU (A_3)	0.071	0.039	1.82	0.0048	0.13	0.02	0.03	12.0
LA (B)	0.095	0.038	2.50	0.0021	0.009	0.001	0.00	10.0

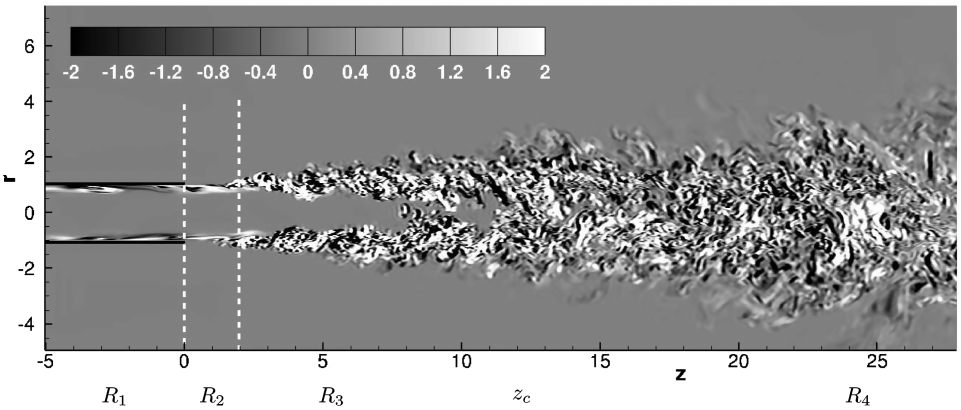

Fig. 8 Contours of instantaneous azimuthal vorticity in the range $|\omega_z| \leq 2$ at cross section $\theta = 0$. Nozzle wall indicated by black bars.

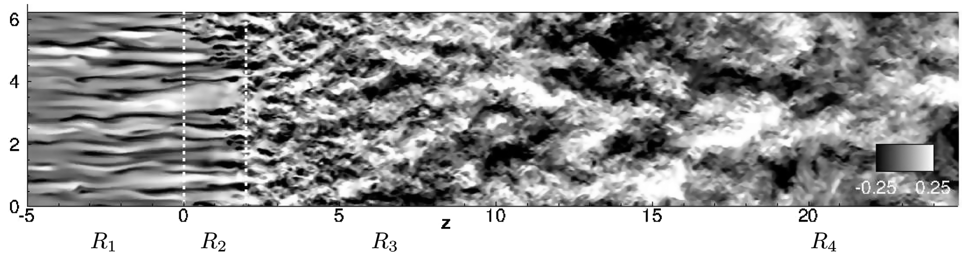

Fig. 9 Contours of instantaneous axial velocity fluctuations on cylindrical surface $y^+ \approx 8$ ($r = 0.98$). Gray scale corresponds to $-0.25 \ldots +0.25$.

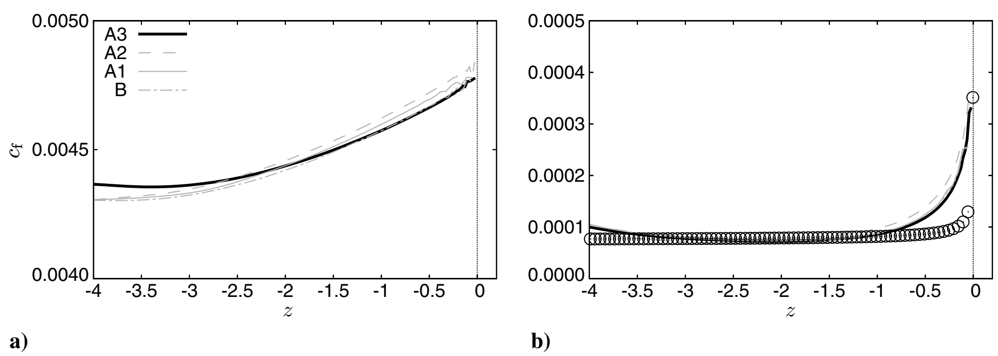

Fig. 10 Development of a) turbulent nozzle boundary layer, and b) laminar boundary layer at outer nozzle wall, characterized by the skin friction $c_f = Re_D \cdot \mu_w \partial\langle w\rangle/\partial r|_w$. Line types of different simulation runs as identified in Fig. 10a.

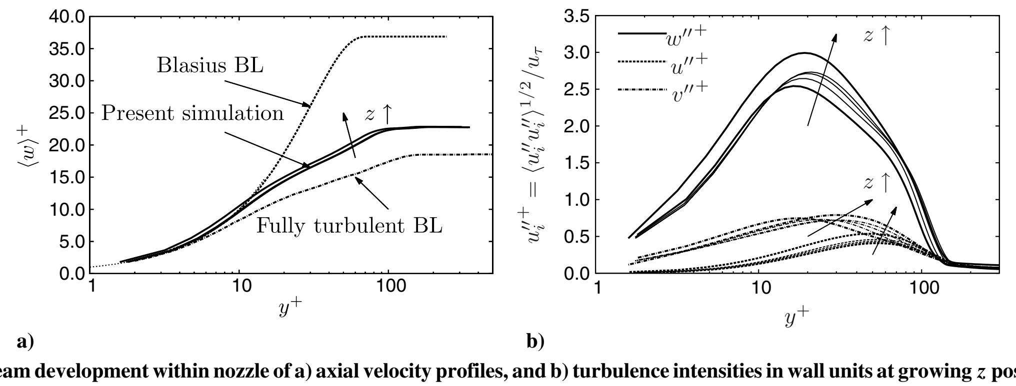

Fig. 11 Downstream development within nozzle of a) axial velocity profiles, and b) turbulence intensities in wall units at growing z positions as indicated by arrows within the axial range −4, −3, −2, −1, 0.

layer. The shape factor $H = 1.82$ of the mean flow profile determined at the nozzle exit is slightly above $H_{\mathrm{turb}} \approx 1.67$ [40] found in a turbulent boundary layer (while $H_{\mathrm{Blasius}} = 2.59$). Further characteristic boundary-layer parameters obtained at the nozzle exit are summarized in Table 2. In conclusion, we obtain a developing turbulent boundary-layer state within our nozzle, which approximates main features of wall turbulence. In view of the variety of possible experimental conditions [57], such an exit boundary layer is of obvious interest in its own right. For future work, a longer nozzle and a higher Reynolds number should be used to study the jet flow arising from a fully developed turbulent exit boundary layer.

3. *Two-Point Correlations and Integral Length Scales*

The two-point autocorrelation for the axial direction is defined as

$$R^z_{jj}(r, z_0 \leqslant z \leqslant z_1; \tilde{z}) = \frac{\langle u_j(\mathbf{x} + \tilde{z} \cdot \boldsymbol{e}_z, t) \cdot u_j(\mathbf{x}, t)\rangle_{t,\theta,[z_0,z_1]}}{\langle u_j(\mathbf{x} + \tilde{z} \cdot \boldsymbol{e}_z, t)^2\rangle^{1/2}_{t,\theta,[z_0,z_1]} \cdot \langle u_j(\mathbf{x}, t)^2\rangle^{1/2}_{t,\theta,[z_0,z_1]}} \tag{4}$$

where u_j $(j = 1, 2, 3)$ denotes the axial, azimuthal, and radial velocity fluctuations, respectively. In Eq. (5), averaging is performed in time, in the azimuthal direction, and within some short axial extent $z_0 \leqslant z \leqslant z_1$ to obtain better statistics. A similar averaging procedure for streamwise-inhomogeneous flows was applied in [54]. Normalized two-point autocorrelations in the circumferential direction are evaluated as

$$R^\theta_{jj}(r, z_0 \leqslant z \leqslant z_1; \tilde{\theta}) = \frac{\langle u_j(\mathbf{x} + \tilde{\theta} \cdot \boldsymbol{e}_\theta, t) \cdot u_j(\mathbf{x}, t)\rangle_{t,\theta,[z_0,z_1]}}{\langle u_j(\mathbf{x} + \tilde{\theta} \cdot \boldsymbol{e}_\theta, t)^2\rangle^{1/2}_{t,\theta,[z_0,z_1]} \cdot \langle u_j(\mathbf{x}, t)^2\rangle^{1/2}_{t,\theta,[z_0,z_1]}} \tag{5}$$

Correlations have been evaluated at the radial position $r = 0.98$ (corresponding to the wall-normal distance $y^+ \approx 8$ at the nozzle exit) in three regions $z_0 \leqslant z \leqslant z_1$: within the developing turbulent boundary layer near the nozzle exit, for $-1 \leqslant z \leqslant 0$, the region of rapid changeover to the turbulent free shear layer, $1 \leqslant z \leqslant 2$, and the initial turbulent shear layer, $5 \leqslant z \leqslant 6$.

Figure 12a shows the correlation coefficients R^z_{jj}. Thin lines denote two-point correlations at growing z positions (indicated by the arrows) within the respective axial ranges ($z = -1, -0.75, \ldots, z = 1, 1.25, \ldots$ and $z = 5, 5.25, \ldots$). The thick lines indicate averages within the respective intervals $z_0 \leqslant z \leqslant z_1$. As expected, axial fluctuations in the buffer layer $5 \leqslant y^+ \leqslant 30$ are correlated over a large axial distance due to the presence of near-wall streaks. The correlation length is found to decrease downstream of the nozzle exit before starting to increase again in the developing shear layer. A clear minimum is present at $\tilde{z} \approx 0.25$ for the radial and azimuthal velocity fluctuations downstream of the nozzle exit, $1 \leqslant z \leqslant 2$. In the developing shear layer $5 \leqslant z \leqslant 6$, the velocities start to become uncorrelated for separations $\tilde{z} \gtrsim 2$. In Fig. 12b, we present two-point autocorrelations in the azimuthal direction for axial velocity fluctuations. The correlations within the nozzle, for $-1 \leqslant z \leqslant 0$, show a minimum $R^z_{ii} \approx 0.35$ around $\widetilde{r\theta}^+_{\mathrm{min}} \approx 125$ marked by an arrow and a maximum $R_{ii} \approx 0.50$ around $\widetilde{r\theta}^+_{\mathrm{max}} \approx 180$. The minimum indicates the spacing of near-wall streaks.

Based on two-point correlations defined in Eqs. (4) and (5), with R_{11} evaluated for $z_0 = z_1$, we compute axial and azimuthal integral length scales by [15]

$$L^z_{11}(z) = \int_0^{\tilde{z}^{0.02}_{11}} R^z_{11}(z, \tilde{z})\,\mathrm{d}\tilde{z} \quad \text{where } R^z_{11}(z, \tilde{z}^{0.02}_{11}) = 0.02 \tag{6}$$

and

$$L^\theta_{11}(z) = \frac{1}{r}\int_0^{\pi/4} R^\theta_{11}(z, \widetilde{r\theta})\,\mathrm{d}\widetilde{r\theta} \tag{7}$$

respectively. Their downstream development is shown in Fig. 13a. Within the nozzle, axial length scales strongly increase within the developing turbulent boundary layer due to the appearance of near-wall streaks. A maximum of $L^{z}_{11}{}^+ \approx 460$ is reached toward the nozzle exit. Length scales then show a sharp drop as near-wall streaks break up in the changeover region (cf. Fig. 9). The behavior of the azimuthal length scales (cf. Fig. 13b) is different. The azimuthal length scale within the nozzle $L^{\theta}_{11}{}^+ \approx 100$ remains constant and no dropoff is observed downstream of the nozzle exit. The smallest scales within the flowfield are immediately present after the nozzle exit, $L^\theta_{11,\mathrm{min}} \approx 0.30$. Within the jet shear layer, azimuthal length scales increase linearly from $L^\theta_{11} \approx 0.30$ at the nozzle exit toward a value of $L^\theta_{11} \approx 0.50$ around $z = 10$, as found also for the axial length scales. Absolute values for the integral length scales obtained in this work are larger than the ones presented in [21], consistent with the fact that a significantly higher Reynolds number of $Re_D = 10^5$ has been studied there.

Besides the physical insight into the turbulent flow development, integral length scales were also used to assess the appropriateness of grid resolution of the different simulation runs. Similar ratios between streamwise integral length scales and grid spacings were reported for the jet-flow simulations of [21], whereas our relative azimuthal resolution is significantly higher. The data are collected in Table 1.

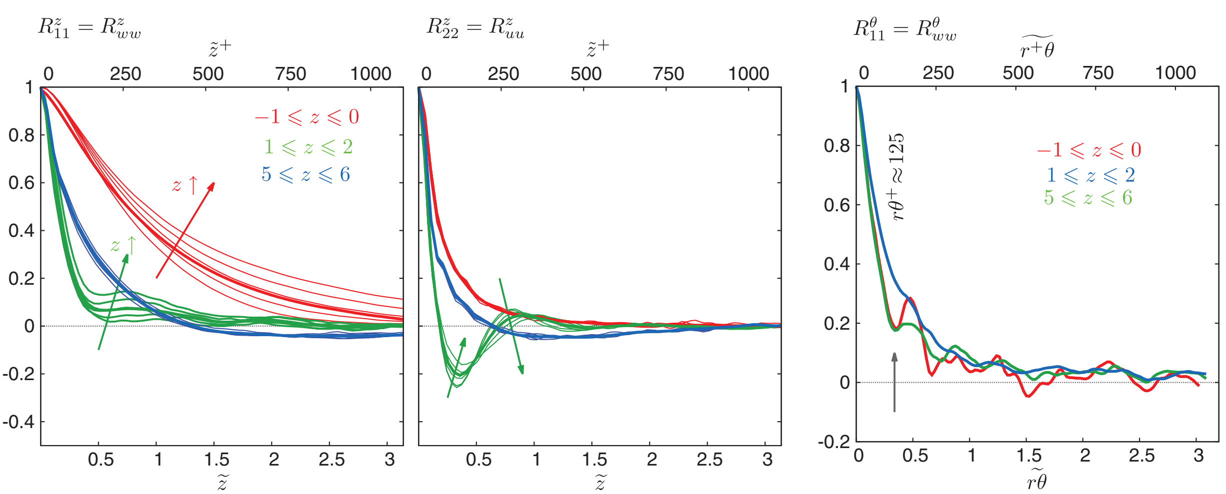

a) b)

Fig. 12 a) Two-point autocorrelations R^z_{jj} evaluated in the downstream direction $\tilde{z}$ within flow regions $R_1 - R_3$ at $y^+ = 8$ (see Fig. 8) and b) two-point autocorrelations $R^\theta_{ww} = R^\theta_{11}$ evaluated in azimuthal direction (spatial averages only).

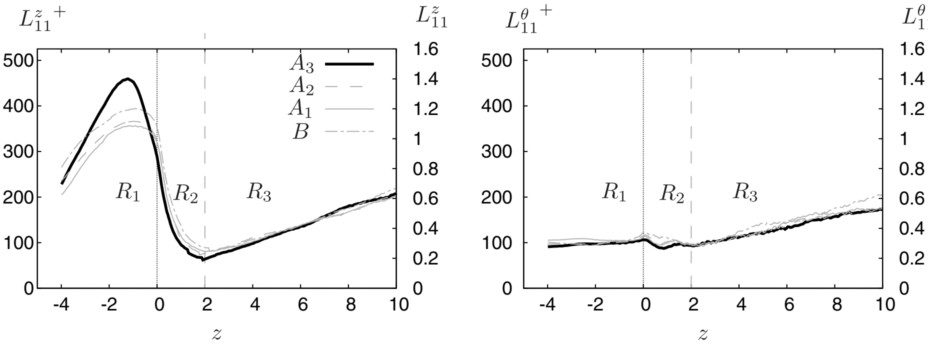

a) b)

Fig. 13 Downstream development of a) axial, and b) azimuthal integral length scales within regions $R_1 - R_3$ at $r = 0.98$. Data from different simulation runs (cf. Table 1).

4. Velocity Spectra

Figure 14 shows azimuthal spectra of the axial velocity at $r = 0.98$ determined by averaging again within a short axial extent $z_0 \leqslant z \leqslant z_1$ as well as local spectra within the respective range. The averaging had only limited influence on the results. All spectra show a decay of amplitudes by at least one decade. For wave numbers beyond $n \geqslant 80$ the action of the filter necessary for stable time-integration (see Sec. II.A) is visible. Within the developing turbulent boundary layer $-1 \leqslant z \leqslant 0$, a flat maximum is observed around $n \approx 9$, which can again be related to the near-wall streaks. It is found in the two-point correlations for the axial velocity (see Sec. III.A.3) that the spacing between streaks in the azimuthal direction is on the order of $\lambda^+/2 \approx 125$, which correspond to $\lambda/2 \approx 0.35$ and explains the dominance of $n \approx 9 \approx 2\pi r/\lambda$. Further downstream within $1 \leqslant z \leqslant 2$, the flat peak is reduced and is not observed in the fully developed turbulent jet in $25 \leqslant z \leqslant 30$. Figure 15 shows temporal power spectral densities (PSDs) determined for axial and radial velocity fluctuations using the Welch algorithm [58] (see the Appendix). Spectra are given at the axial locations $z = 0, \ldots, 4$ downstream of the nozzle-exit plane. Axial velocity spectra in the nozzle-exit plane $z = 0$ show that no particular frequency is triggered inside the nozzle using our inflow boundary treatment. A decay is observed for frequencies higher than $St_D \approx 0.1$. Further downstream, this decay is reduced, and we obtain a slight peak around frequencies $St_D \approx 0.3$. At $z = 3$ and $z = 4$, spectral amplitudes within the frequency range $0.2 \leqslant St_D \leqslant 0.3$ become slightly dominant. PSDs of radial velocity fluctuations show a peak immediately after the nozzle exit $z = 1$ around $St_D \approx 1.2$. Further downstream, radial fluctuations pick up more and more energy, and spectral amplitudes increase. In addition, peak levels are shifted toward lower frequencies as it has also been observed in [21]. The spectral peaks are much less pronounced than for laminar or transitional nozzle-exit conditions studied in [22] whose peak-frequencies correspond to the most amplified modes of linear stability theory (LST) for local mean-flow profiles. This is probably related to the fact that turbulence levels in the beginning free shear layer are significantly higher for a turbulent nozzle boundary layer invalidating application of LST.

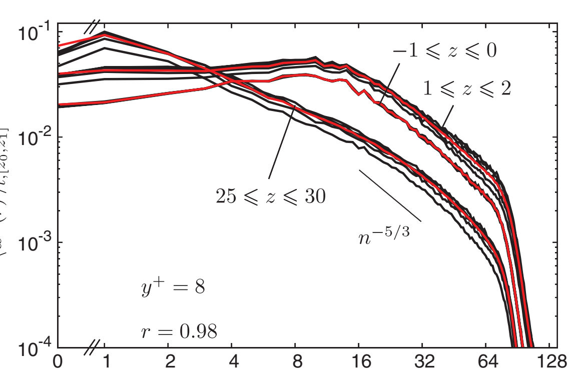

Fig. 14 Azimuthal spectra of axial velocity fluctuations at $y^+ = 8$, averaged in time and over different axial extents (red lines) as indicated. Black lines denote local spectra within the respective axial ranges ($z = -1, -0.75, \cdots, z = 1, 1.25, \cdots$ and $z = 25, 26, \cdots$).

5. Impact of Grid Resolution and Computational Domain Size

The main focus of the simulation runs A_1–A_3 (cf. Fig. 4) is to study possible resolution effects on the development of the turbulent nozzle boundary layer and its changeover to the turbulent free shear layer. As can be seen in Fig. 10, only minor differences are found for the skin friction. The aim of the grid refinement in the vicinity of the nozzle trailing edge (simulations A_2 and A_3) is to capture a potential skin friction increase [56]. Although the resolution is significantly refined, a strong increase of c_f was not obtained for our boundary layer inside the nozzle. This may be related to the presence of a pressure gradient in the circular pipe (not considered in the analytical model [56]) and the fact that we do not reach a fully developed turbulent flow state in our short nozzle. A strong increase of c_f is found for the outer (laminar) boundary layer, Fig. 10b.

Integral length scales in the axial direction (Fig. 13) reach highest levels within the nozzle for simulation run A_3 applying the finest near-wall resolution. They are predicted somewhat lower in the runs

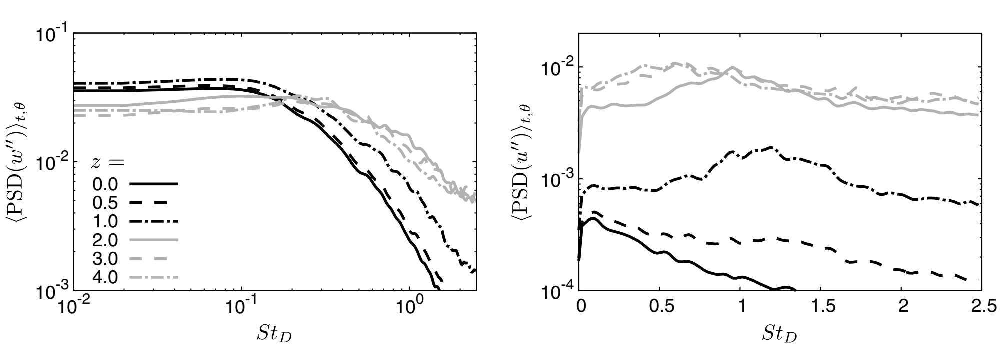

a) b)

Fig. 15 Temporal spectra of a) axial, and b) radial velocity fluctuations on a cylindrical surface $r = 0.98$ ($y^+ = 8$) within regions R_2 and R_3 (see Fig. 8).

A_1, A_2, and B. However, the general development within the nozzle is similar in all simulation runs. Integral length scales in the subsequent jet flow are in very close agreement, as are the azimuthal integral length scales.

To investigate effects of resolution and box size (simulation run B) in more detail, an additional comparison of mean flow and rms profiles at the nozzle exit is given in Fig. 16. These data agree well for all simulation runs. The lower resolution chosen in runs A_1 and B (with the first grid point away from the wall located at $\Delta r_w^+ \approx 3$ and an azimuthal resolution of $R^+\Delta\theta \approx 15$) is capable of reproducing the turbulent flow development reasonably well. Grid refinement in the axial direction (run A_2) and the azimuthal direction (run A_3) by a factor of 2 had no significant influence on the flow profiles.

A comparison of temporal axial velocity spectra is given in Fig. 17 within the turbulent boundary layer at $(r, z) = (0.98, 0)$. Spectral amplitudes found in the simulation runs A_1, A_2, and B applying the same number of azimuthal grid points $N_\theta = 128$ are lower than those of case A_3 with $N_\theta = 256$. However, we will see that this has little influence on the sound spectra discussed in Sec. III.C. Azimuthal spectra of axial velocity fluctuations are compared in Fig. 17. In the free shear layer, spectra are in rather good agreement for all simulation runs up to the wave numbers modified by the action of the filter. The filter cutoff depends on the chosen azimuthal resolution corresponding to $n_c \approx 2/3 \cdot N/2 \approx 40$ for simulation runs A_1, A_2, and B ($N_\theta = 128$) and $n_c \approx 80$ in simulation run A_3 ($N_\theta = 256$) as indicated by the thin dashed line in Fig. 17b. The resolution applied in A_3 shows a decay in spectral amplitudes of roughly one decade before the action of the filter sets in. In the simulation runs A_1, A_2, and B, the effect of the azimuthal filter on the simulation results is found to be similar to the effect of filtering applied in the LES of [9,10].

B. Overall Nozzle Jet Flowfield

Next, we discuss the overall flowfield development in the whole computational domain. We consider the mean flow and turbulent fluctuations, adding brief comparisons to results for laminar nozzle-exit conditions; see Table 2.

Figure 18 shows the downstream development of the mean axial velocity (Fig. 18a) and the rms fluctuations (Fig. 18b) in the nozzle, changeover, and the beginning jet region. The dashed line in Fig. 18a denotes the development of the jet half-width $r_{1/2}$. The boundary layer with thickness $\delta = 0.3$ introduced at the inflow develops gradually along the wall. As its thickness increases, the flow in the core region is slightly accelerated toward the end of the nozzle (as will also be seen in Fig. 19, left). The boundary layer at the outer nozzle wall has only weak influence on the flow profiles downstream the nozzle exit. The jet half-width $r_{1/2}$ (dashed line) remains constant downstream of the nozzle exit and grows only downstream of the end of the potential core z_c, finally reaching $r_{1/2} = 1.8$ at $z = 30$. The rms profiles in Fig. 18b show that axial fluctuation levels rise within the nozzle and agree reasonable well at $z = -1$ with those of [40] introduced at the inflow. Downstream of the nozzle the fluctuations spread out rapidly in the radial direction. Within the initial development region of the jet shear layer, $0 \leqslant z \leqslant 4$, the fluctuation levels increase, compared to their values in the nozzle-exit plane.

In Fig. 19a, the downstream development of the centerline velocity (normalized by the nozzle exit velocity) is shown. For the turbulent exit conditions, the potential core is closed at $z_c \approx 12$ when defined by the axial position where $\langle w\rangle/\langle w\rangle_{\mathrm{cl}} = 0.95$ as indicated by the dashed lines. Compared to measurements of a $Ma = 0.9$ jet [59], the potential flow core is slightly shorter in our simulations, which is possibly related to a substantially higher Reynolds number ($Re_D \approx 10^6$) in the experiment. Figure 19b shows the development of the shear-layer momentum thickness. It grows nearly linearly downstream of $z = 2$. This is also the axial position where the axial integral length scale, previously discussed in Fig. 13, starts growing. For laminar nozzle-exit conditions, the potential flow core is shorter by approximately one nozzle diameter, and the decay of the centerline velocity is significantly enhanced. The momentum thickness increases more slowly in the beginning of the jet-flow development but more strongly downstream.

The rms fluctuation levels along the centerline and radial maxima are given in Fig. 20 for the axial and radial components. Fluctuation levels along the centerline start to increase slowly after the nozzle

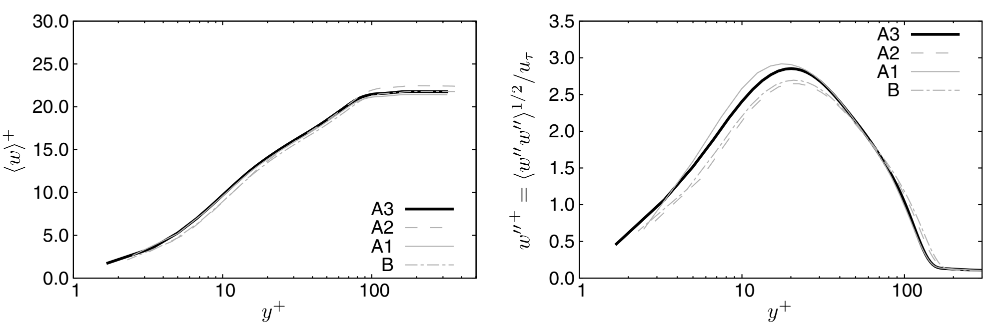

a) b)

Fig. 16 Comparison of a) axial velocity profiles, and b) axial turbulence intensities in wall units at nozzle exit $z = 0$ for the different simulation runs.

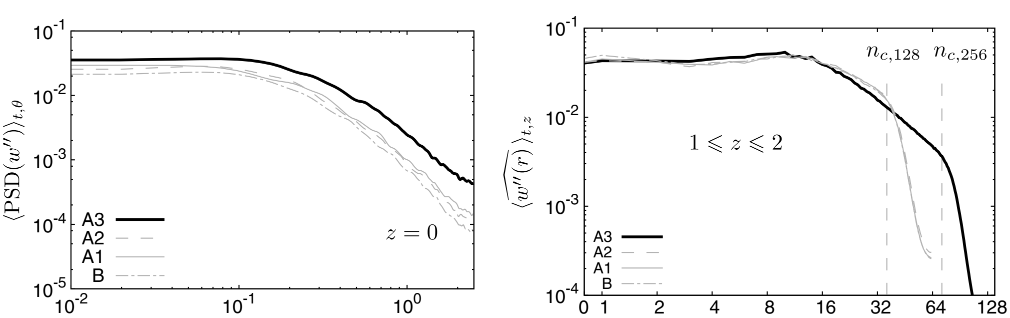

a) b)

Fig. 17 a) Temporal spectra of axial velocity fluctuations along $r = 0.98$ ($y^+ = 8$) at nozzle-exit plane $z = 0$. b) Azimuthal spectra of axial velocity fluctuations within the beginning turbulent free shear layer along $r = 0.8$ ($y^+ = 8$).

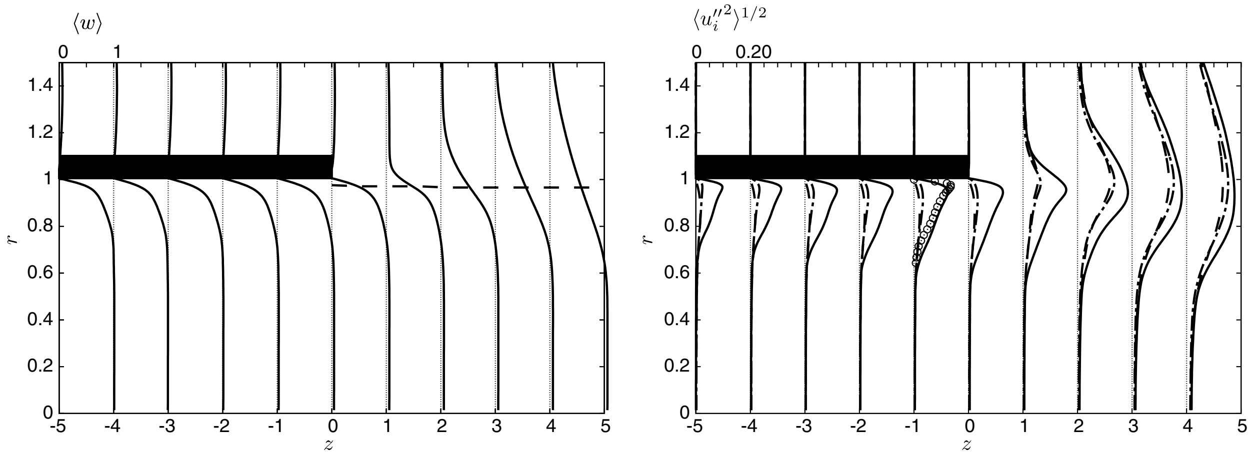

a) b)

Fig. 18 Development of a) mean axial velocity profiles $\langle w \rangle$, and b) rms fluctuations $\langle u_{i''}^2 \rangle^{1/2}$ at various axial locations. ——— $\langle w''^2 \rangle^{1/2}$, - - - - - - $\langle u''^2 \rangle^{1/2}$ and -·-·-·- $\langle v''^2 \rangle^{1/2}$. ⊙ SEM reference profile [40] $\langle w''^2 \rangle^{1/2}_{\mathrm{ref}}$ displayed at axial location $z = -1$ for comparison.

exit and in a more pronounced way toward the end of the potential core. Compared to the experiment [59], this rise is slightly shifted upstream, likely due to the shorter potential flow core mentioned already. However, our peak levels for axial and radial fluctuations attained at $z \approx 17$ agree rather well with the measurements [59], as does the general rms development further downstream. Axial rms fluctuations jump from $\max_r \langle w''^2 \rangle^{1/2} \approx 0.13$ at the nozzle exit (cf. Fig. 18) to ≈0.18 in the initial free shear layer. The rapid

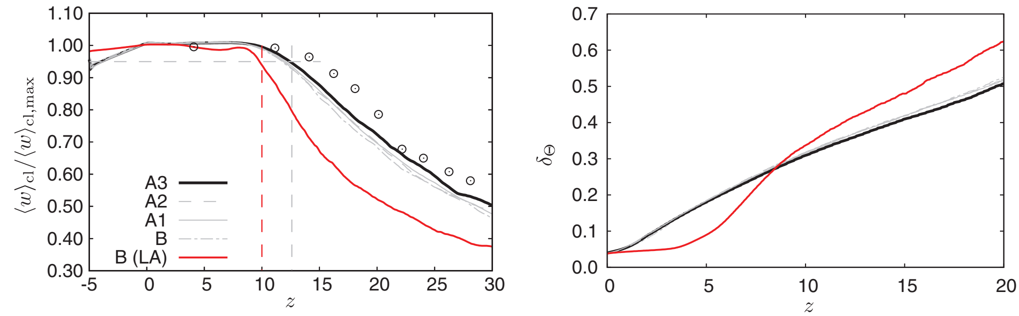

a) b)

Fig. 19 Development of a) centerline velocity and b) momentum thickness. Red: laminar nozzle boundary layer. Circles denote measurements of [59] for a $Ma = 0.9$ jet.

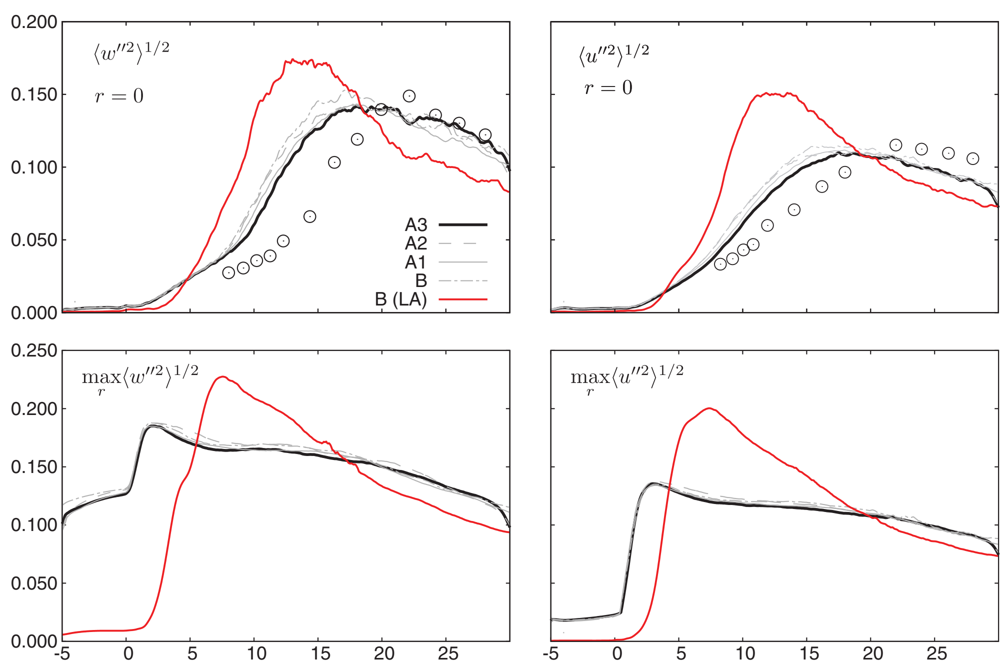

Fig. 20 Development of axial (left) and radial (right) velocity fluctuations along $r = 0$ (top row) and radial maxima (bottom row). Red: laminar nozzle boundary layer. Circles denote measurements of [59] for a $Ma = 0.9$ jet.

increase is even more pronounced for the maximum radial fluctuations, from $\max_r \langle u''^2 \rangle^{1/2} \approx 0.02$ at the nozzle exit to ≈ 0.14 just slightly downstream. The peak observed in both axial and radial fluctuations might be related to the low Reynolds number of our jet flow, while a higher Reynolds number jet flow [60] shows no such peak.

Again, data are compared to results for laminar nozzle-exit conditions. Obviously, the peak arising along the centerline is strongly enhanced when the nozzle-exit turbulence level is decreased. This corresponds to the frequent observation that fluctuations are stronger during transition than in the fully developed turbulent flowfield. In addition, we observe a peak-shift upstream, related to the shorter potential flow core (cf. Fig. 19). The peak in radial maxima is found to be strongly enhanced as well, whereas the peak location is now shifted downstream. This is related to the fact that fluctuations are low immediately downstream of the nozzle-exit fluctuations and grow only during laminar–turbulent transition initiated by a Kelvin–Helmholtz shear-layer instability.

Regarding the effects of grid resolution and computational domain size, very close agreement is found for the centerline velocity (Fig. 19), the turbulence statistics along centerline, and radial maxima (Fig. 20).

The downstream development of the mean axial velocity profiles in similarity coordinates $\langle w \rangle / \langle w_{\mathrm{cl}} \rangle (r/r_{1/2})$ is shown in Fig. 21a. The nozzle-exit ($z = 0$) profile also shows the outer nozzle-wall boundary layer with a maximum velocity $\langle w \rangle / \langle w_{\mathrm{cl}} \rangle \approx 0.06$. Further downstream, the profile shape changes rapidly, and beyond $z = 16$, all profiles collapse and are in close agreement with the theoretical solution [51]. The attained self-similar state suggests correct entrainment into the jet by the boundary treatment of our computational setup. Figure 21b shows the development of turbulent kinetic energy (TKE) profiles. Within the jet, TKE profiles first show a rapid increase in the shear layer downstream of the nozzle exit and attain their similarity shape at $z \approx 20$.

C. Acoustic Near Field

1. *Instantaneous Flow and Pressure Field*

To get an overview of the overall turbulent nozzle jet-flow development and the acoustic field, Fig. 22 shows contours of the instantaneous vorticity magnitude and the near-field pressure distribution. The dashed line in (a) delimits the region outside which sponge layers are active (cf. Fig. 1). Coherent structures identified by the regular pressure contours in the vicinity of the jet shear layer are traveling downstream with the jet. Apart from these hydrodynamic pressure waves, acoustic pressure waves are visible in the near field of the jet. Figure 22b illustrates that sound waves are emitted from the turbulent shear layer in the sideline direction immediately downstream of the nozzle exit and from a region further downstream around $z = 5$ (Fig. 22a). We do not observe significant spurious reflections of pressure waves at the inflow, nor at the far-field or outflow boundaries. This indicates an appropriate boundary treatment through the

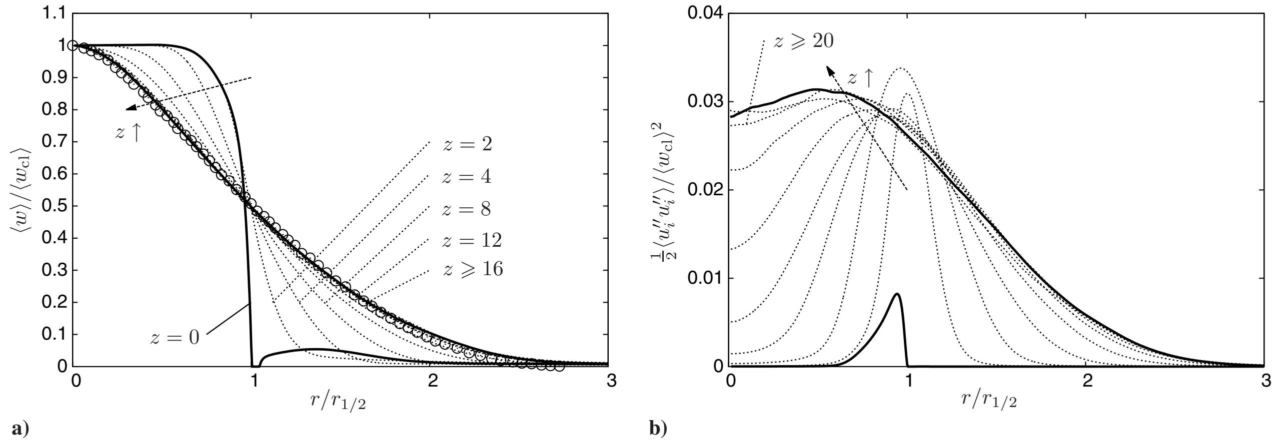

Fig. 21 Downstream development of a) mean axial velocity, and b) radial profiles of turbulent kinetic energy in similarity coordinates. Circles denote the self-similar solution [51] for incompressible round jets.

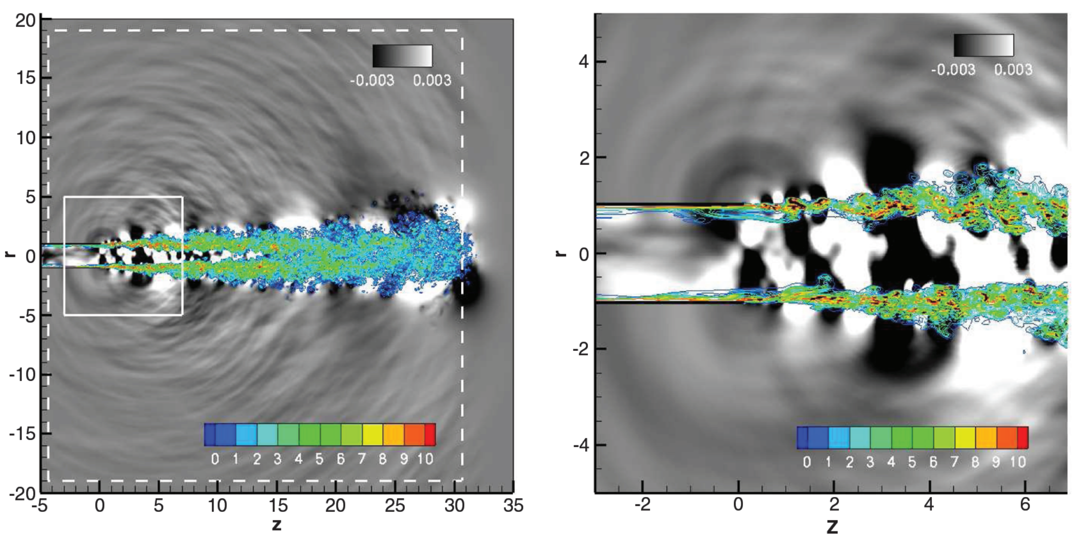

Fig. 22 Visualization of instantaneous vortical structures by contours of vorticity magnitude $|\omega|$ (color scale), and pressure waves emitted by contours of pressure fluctuations p'' (gray scale): a) total simulation domain, and b) close-up of nozzle-exit region.

sponge layers in combination with the nonreflecting boundary conditions. With the axial grid stretching downstream of $z = 30$, fine-scale turbulent structures are no longer represented on the computational grid, and fluctuations are damped in the sponge layer, such that a proper functioning of the nonreflecting boundary conditions is supported.

2. Near-Field Sound Spectra

In this section, we present near-field acoustic pressure spectra and compare them with experimental data [61] obtained for the much higher Reynolds number $Re_D = 7.8 \cdot 10^5$ at the four microphone positions in Fig. 3 ($r = 15$, $z = 0, 10, 20, 25$). We also briefly compare the pressure spectra to our results for laminar nozzle-exit conditions.

We recorded pressure time signals in the acoustic near field and computed the corresponding sound pressure levels (SPLs) using the Welch algorithm [58] (as detailed in the Appendix). Grid spacings for the axial and radial directions in the acoustic near field were chosen to represent acoustic pressure waves up to Strouhal number $St_D = f^\diamond D^\diamond / w^\diamond_{\mathrm{cl}} = 2$ with at least 10 grid points per wavelength.

The computational data and their comparison with experimental data are presented in Fig. 23 ($\varphi^\star$ denotes the emission angle with respect to $(r, z) = (0, 0)$). For the noise emitted in the directions $\varphi^\star = 40$ and 60 deg, we find quite a good agreement between measurement and simulation data over the whole frequency range. At $\varphi^\star = 60$ deg, SPLs are predicted to be about 1–2 dB higher at all frequencies. At $\varphi^\star = 30$ deg (where no reference data are available) and $\varphi^\star = 40$ deg, a flat peak is observed at $St_D = 0.2$. In the sideline direction, $\varphi^\star = 90$ deg, some differences are visible. In the frequency range $0.5 \leqslant St_D \leqslant 1.5$, the SPLs are predicted to be $\approx$2–3 dB higher in all of our simulation runs. This might be related to the presence of a peak in the axial and radial rms fluctuations previously found in Fig. 20 downstream of the nozzle exit within the jet shear layer. An overprediction is also present in the low-frequency range $0.1 \leqslant St_D \leqslant 0.25$, for the simulation runs A_1–A_3 for which we use the smaller computational box size, while run B with the larger box reproduces the experimental result very well. An explanation is given in Sec. III.C.4.

The strong influence of the nozzle-exit turbulence level on sound emission becomes particularly obvious when we compare our simulation results for laminar and for turbulent nozzle-exit conditions. As seen in Fig. 23, the SPLs for the laminar case are about 6 dB higher at nearly all emission angles and frequencies. At $\varphi^\star = 30, 60$ deg, in addition to higher SPLs a pronounced peak is apparent at Strouhal number around $St_D \approx 0.35$, most probably related to strong vortex pairing in the jet shear layer (see [21]). To get further insight into this issue a detailed comparison of laminar, transitional and turbulent nozzle-exit conditions is carried out in separate work [22].

3. Scaling of Sound Pressure Level with Reynolds Number and Turbulence Level

The overall close agreement of our simulation data for turbulent nozzle-exit conditions with the experimental data of [61] was not to be expected as the latter study was carried out at a substantially higher Reynolds number. To find a possible explanation, we consider the SPL dependence on Reynolds number Re_D and turbulence level $\mathrm{Tu} = \max_r \langle w'^2 \rangle^{1/2}$ $(z = 0)$ presented in [60] (Tu = 9%) and [21] ($Re_D = 10^5$), respectively. These data show that the effect of a higher Reynolds number may be compensated at least partially by a reduced turbulence level. The overall sound pressure levels (OASPLs) found in [21,60] are plotted in Figs. 24a and 24b for different emission angles $\varphi^\star$. A suitable fit to the data of Fig. 24a is

$$\mathrm{SPL}(\mathrm{Tu}) = a_{\mathrm{Tu}} \cdot \log(\mathrm{Tu}) + b_{\mathrm{Tu}} \tag{8}$$

with slopes a_{Tu} dependent on $\varphi^\star$. Similarly, the data of Fig. 24b are represented by

$$\mathrm{SPL}(Re_D) = \begin{cases} a_{Re} \cdot \log(Re_D) + b_{Re}, & Re_D \leqslant Re_{D,\max} \\ \mathrm{SPL}(Re_{D,\max}) \qquad , & Re_D > Re_{D,\max} \end{cases} \tag{9}$$

where the OASPLs do not change beyond some $Re_{D,\max}$, $=2 \cdot 10^5$ ($\varphi^\star = 40$ deg) and $=1 \cdot 10^5$ ($\varphi^\star = 60$ deg and $\varphi^\star = 90$ deg). Assuming that relations (8) and (9) both fit the experimental data [61] as well, we obtain the same sound pressure levels as [61] at the conditions of our simulation ($Re_D = 18100$, Tu = 13%) for an experimental turbulence level of Tu $\approx$ 7%. This value is well within the range present in experimental investigations [62]. Thus, the

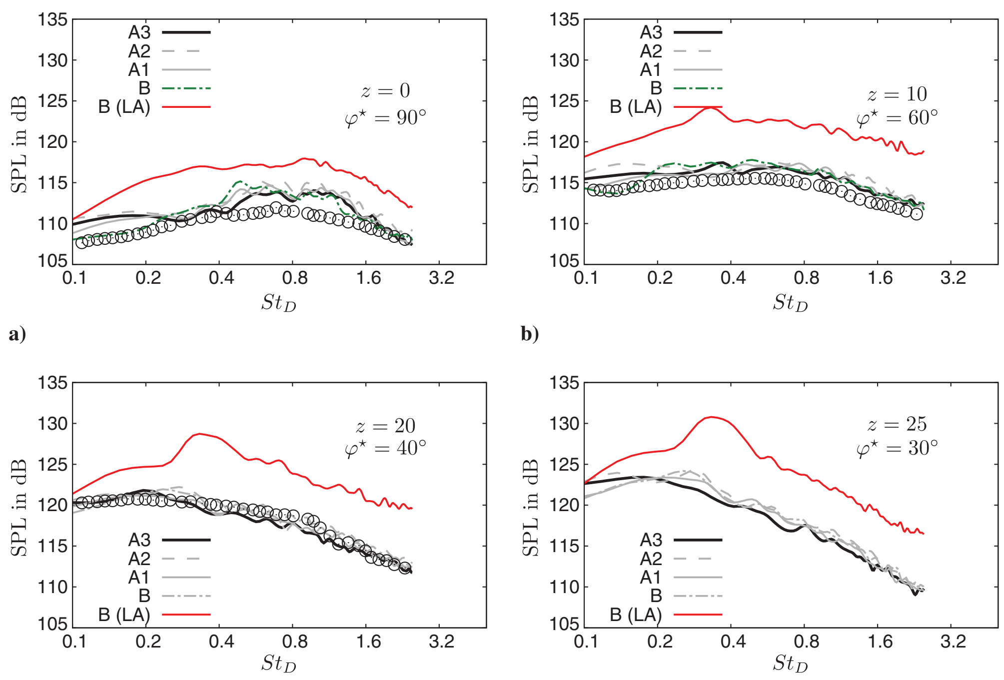

Fig. 23 Near-field sound pressure levels as a function of Strouhal number St_D at $r = 15$ and different axial positions z (cf. Fig. 3). $\varphi^\star$ denotes the emission angle with respect to $(r,z) = (0,0)$. Line types as identified in Fig. 23a. Red: laminar nozzle boundary layer. Circles represent near-field measurements [61].

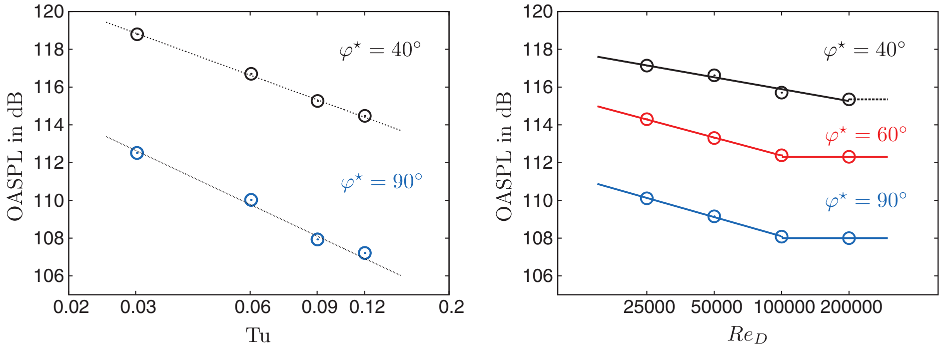

a) b)

Fig. 24 OASPL as a function of a) turbulence level and b) Reynolds number. Circles denote data of [21,60]. Data fit according to Eqs. (8) and (9) with parameters depending on $\varphi^\star$: $a_{Tu,90\ \mathrm{deg}} = -4.13$ and $a_{Tu,40\ \mathrm{deg}} = -3.21$; $a_{Re,90\ \mathrm{deg}} = -1.46$, $a_{Re,60\ \mathrm{deg}} = -1.38$, and $a_{Re,40\ \mathrm{deg}} = -0.91$.

compensation effect expressed by relations (8) and (9) may well provide an explanation for the good agreement between our simulation and the experimental data despite the large discrepancy in the Reynolds numbers.

Using correlation (8), we may also try to scale the SPL results of our simulation with laminar nozzle-exit conditions (Tu = 0.9%, Table 2) to our simulations with turbulent conditions. The scaled SPL is presented in Fig. 25 (broken red line) together with our turbulent-case simulation data (solid black line) and those of the reference experiment [61]. Although sound spectra in the laminar case have a different character, the scaling relation [Eq. (8)] brings SPLs closer to the turbulent-case data. We conclude that the scaling using relations [Eqs. (8) and (9)] may work reasonably well for both laminar and turbulent nozzle-exit conditions.

4. *Impact of Grid Resolution and Computational Domain Size*

A comparison of near-field sound spectra for the various simulation runs with different grid resolutions (case A_1–A_3) and box sizes (case B) is also included in Fig. 23. Only minor differences are observed among runs A_1–A_3, and they are in the same range as those

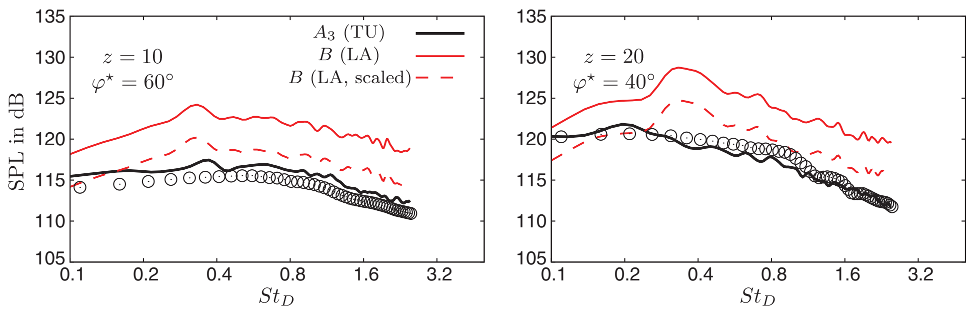

a) b)

Fig. 25 Near-field sound pressure levels as a function of Strouhal number St_D at $r = 15$. Line types as identified in Fig. 25a; broken line shows SPL scaled by Eq. (8).

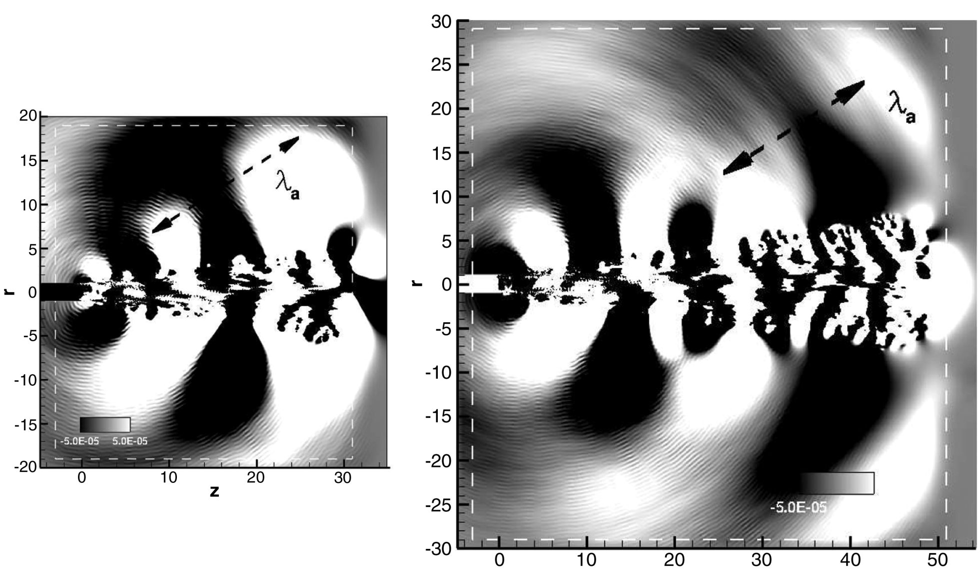

Fig. 26 Near-field pressure wave at $St_D = 0.1$ visualized by $Re\{\mathcal{F}_t(p)\}$ in the two-dimensional plane $\theta = 0$. Simulation run A_3 (left) and run B (right). The arrow denotes the acoustic wavelength $\lambda_a = 2/(St_D \cdot Ma)$.

obtained for the grid resolution study presented in [16]. Small differences between A_1–A_3 and B present in the low-frequency range for the sideline direction (Fig. 23a) are likely due to the larger domain size rather than due to the resolution (simulation B has the same resolution as A_1 within the nozzle and the jet shear layer). This can be related to the fact that low-frequency/long-wavelength acoustic pressure waves are clearly better represented in the larger computational domain of simulation B, as visualized in Fig. 26 by a temporal Fourier transform of the pressure fluctuations.

IV. Conclusions

We performed direct numerical simulations of a nozzle jet flow at Mach number 0.9 including the acoustic near field. The flow inside the nozzle of 2.5 diameters length consists of a developing turbulent wall boundary layer with a potential flow core. The boundary-layer thickness at the nozzle inflow was chosen as $\delta = 0.3$ radii. As a consequence, the corresponding lowest jet Reynolds number for which the nozzle boundary layer is turbulent is $Re_D = 18,100$ ($Re_\Theta = 300$ following [40]). The turbulent boundary layer at the inflow to the nozzle was triggered using the synthetic-eddy method (SEM) [25–27]. The boundary layer along the inner nozzle-wall shows the main features of developing wall turbulence. Axial velocity fluctuations reach peak levels of $\langle w''^2 \rangle_{\max}^{1/2} \approx 13\%$ at the nozzle-exit plane and up to $\approx$18% within the free shear layer. For such a simulation, the simultaneous resolution of near-wall turbulence within the nozzle and the acoustic near field is a particular challenge.

Accuracy of the numerical results has been confirmed by varying the grid resolution and the computational domain size. The comparison of flow statistics, velocity spectra, and sound pressure levels shows only minor differences between the highly resolved simulation (run A_3) and the marginally resolved simulations (A_1, A_2, and B). Generally, a lack of full resolution of the fine-scale turbulence is not considered to be crucial for predicting the dominant part of the noise spectrum [37]. This statement is consistent with our results.

Near-wall turbulent streaks present within the nozzle are found to break down into smaller structures within a changeover region of about one diameter length downstream of the nozzle trailing edge. Accordingly, integral axial length scales of turbulence show a sharp decay downstream of the nozzle exit before slowly increasing linearly in the axial direction z during the further jet development. Integral azimuthal length scales, slowly increasing with z as well, are roughly of the same order as axial length scales within the jet. A self-similar jet flow is attained beyond 10 diameters downstream of the nozzle exit. The mean axial velocity in similarity coordinates is in good agreement with the theoretical solution [51] for incompressible flows using a turbulent mixing-length model.

Considering the development of the acoustic near field, we do not observe any strong nozzle-based sound sources as they were present in [20]. A likely reason for this difference is our use of the non-reflecting boundary conditions and a sponge layer at the inflow. As a main result of this investigation, the near-field sound pressure levels (SPLs) evaluated for radiation angles $\varphi^\star = 40$, 60, and 90 deg are in close agreement with experimental reference data, despite our much lower Reynolds number. This agreement is attributed essentially to a compensation of the effects of our lower Reynolds number and higher nozzle-exit turbulence level. This was confirmed to be plausible by employing a corresponding SPL scaling derived from data of previous studies [21,60].

The effect of nozzle-exit turbulence level on sound emission has been briefly addressed also by comparison with results for a laminar nozzle-exit boundary layer with the same initial shear-layer thickness. Compared to the turbulent case, we find enhanced sound radiation by up to 6 dB at nearly all emission angles and frequencies. In addition, the scaling procedure applied in the laminar inflow case at radiation angles $\varphi^\star = 40$ and 60 deg brings the SPL in closer agreement. A more detailed study of the impact of laminar, transitional, and turbulent nozzle-exit conditions on jet flow and noise at $Re_D = 18,100$ is presented in [22].

Regarding our resolution study, we conclude that all of our computational grids properly capture the jet-flow development as well as the acoustic near field. We consider simulation run B (applying the larger computational domain size) to best represent the low-frequency long-wavelength acoustic pressure waves and therefore the near-field sound in general. To get closer to a fully developed turbulent nozzle boundary layer, a choice of a longer nozzle, higher Re_Θ, and still better radial near-wall resolution would be advisable in future work.

Appendix A: Computing Temporal Spectra Using Welch's Method

The power spectral density P of the pressure signal $p(t)$ is related to the variance $\langle p''p'' \rangle$ by Parseval's identity, which states that the signal power can be computed either in the time or the frequency domain:

$$\langle p''p'' \rangle = \frac{1}{T}\int_0^T p''^2(t)\,\mathrm{d}t = \int_0^{St_{\max}} P(St)\,\mathrm{d}St \qquad \text{(A1)}$$

For the computation of P, we use the Welch algorithm [58]. To this end, we subdivide the total time interval $T_{\mathrm{sim}} = 400$ into $N_w = 20$ overlapping time sequences of length $\Delta T_w = 40$. Hann windows are introduced to ensure periodicity in each sequence before computing the FFTs, as illustrated in Fig. A1a, and the resulting spectra are averaged to obtain P. Neighboring windows overlap by 50%. The pressure signals were recorded in time steps of 0.2 to resolve nondimensional frequencies up to $St_D = 2.5$. The SPL is defined as

$$\mathrm{SPL} := 10 \cdot \log\left(P \cdot \frac{p_{\mathrm{cl}}^{\diamond 2}}{p_{\mathrm{ref}}^{\diamond 2}}\right) \cdot \mathrm{dB} \qquad \text{(A2)}$$

The acoustic reference pressure is chosen as $p_{\mathrm{ref}}^{\diamond} = 2 \cdot 10^{-5}$ Pa. Note that the SPL values are sensitive to the chosen window width, shape,

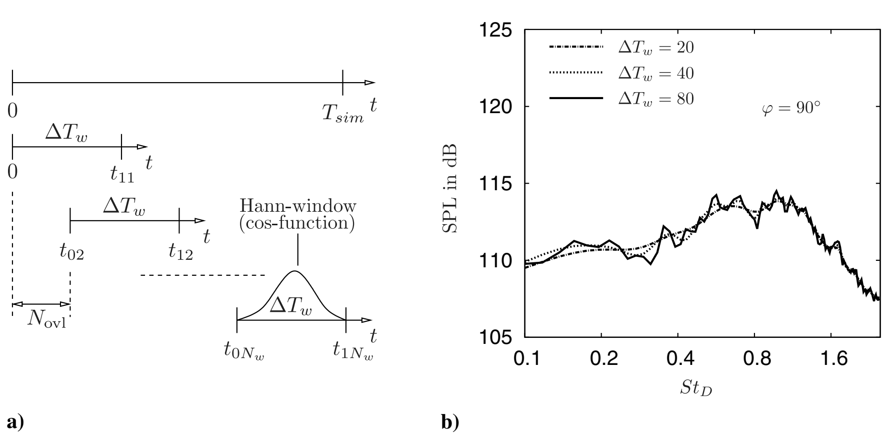

a) b)

Fig. A1 a) Illustration of time record segmentation using the Welch algorithm [58]. b) SPL as a function of Strouhal number for various window lengths ΔT_w and constant overlap of 50%.

and overlap. These data are not always documented well in publications. As an example, the influence of the window width ΔT_w on the computed SPL is visualized in Fig. A1b, which illustrates the obvious smoothing effect of averaging over an increasing number of windows N_w for a given signal length T_{sim}.

Acknowledgments

This work was partially supported by the Swiss National Science Foundation under project number 200020-117926. Computing resources were provided by the Swiss National Supercomputing Center under project ID s52. We would like to thank W. Schneider (Vienna University of Technology) for helpful discussions on entrainment into the jet. We thank as well our colleagues M. Gloor and D. Obrist for valuable discussions and helpful comments.

References

[1] Tam, C. K. W., "Jet Noise: Since 1952," *Theoretical and Computational Fluid Dynamics*, Vol. 10, Nos. 1–4, 1998, pp. 393–495. doi:10.1007/s001620050072

[2] Lilley, G. M., "Jet Noise: Classical Theory and Experiment," *Aeroacoustics of Flight Vehicles*, edited by Hubbard, H. H., Vol. 1, Acoustical Society of America, 1994, pp. 211–289.

[3] Jordan, P., and Colonius, T., "Wave Packets and Turbulence," *Annual Review of Fluid Mechanics*, Vol. 43, Jan. 2013, pp. 173–195. doi:10.1146/annurev-fluid-011212-140756

[4] Freund, J. B., "Noise Sources in a Low-Reynolds-Number Turbulent Jet at Mach 0.9," *Journal of Fluid Mechanics*, Vol. 435, July 2001, pp. 227–305. doi:10.1017/S0022112001004414

[5] Bodony, D. J., and Lele, S. K., "Jet Noise Prediction of Cold and Hot Subsonic Jets Using Large-Eddy Simulation," *10th AIAA/CEAS Aeroacoustics Conference and Exhibit*, AIAA Paper 2004-3022, May 2004.

[6] Bodony, D. J., and Lele, S. K., "Generation of Low Frequency Sound in Turbulent Jets," *11th AIAA/CEAS Aeroacoustics Conference and Exhibit*, AIAA Paper 2005-3041, May 2005.

[7] Bogey, C., and Bailly, C., "Large Eddy Simulations of Transitional Round Jets: Influence of the Reynolds Number on Flow Development and Energy Dissipation," *Physics of Fluids*, Vol. 18, No. 6, 2006, Paper 065101. doi:10.1063/1.2204060

[8] Bogey, C., and Bailly, C., "An Analysis of the Correlations Between the Turbulent Flow and the Sound Pressure Fields of Subsonic Jets," *Journal of Fluid Mechanics*, Vol. 583, July 2007, pp. 71–97. doi:10.1017/S002211200700612X

[9] Keiderling, F., "Direct Noise Computation of High Reynolds Number Subsonic Jet Flow Using LES," ETH Zurich, Rept. 17955, Zurich, 2008.

[10] Keiderling, F., Kleiser, L., and Bogey, C., "Numerical Study of Eigenmode Forcing Effects on Jet Flow Development and Noise Generation Mechanism," *Physics of Fluids*, Vol. 21, No. 4, 2009, Paper 045106. doi:10.1063/1.3112686

[11] Bodony, D., and Lele, S., "Current Status of Jet Noise Predictions Using Large-Eddy Simulation," *AIAA Journal*, Vol. 46, No. 2, 2008, pp. 364–380. doi:10.2514/1.24475

[12] Bogey, C., Bailly, C., and Juvé, D., "Noise Investigation of a High Subsonic, Moderate Reynolds Number Jet Using a Compressible Large Eddy Simulation," *Theoretical and Computational Fluid Dynamics*, Vol. 16, No. 4, 2003, pp. 273–297. doi:10.1007/s00162-002-0079-4

[13] Suponitsky, V., Sandham, N., and Agarwal, A., "On the Mach Number and Temperature Dependence of Jet Noise: Results from a Simplified Numerical Model," *Journal of Sound and Vibration*, Vol. 330, No. 17, 2011, pp. 4123–4138. doi:10.1016/j.jsv.2011.02.007

[14] Suponitsky, V., Sandham, N., and Morfey, C., "Linear and Nonlinear Mechnisms of Sound Radiation by Instability Waves in Subsonic Jet," *Journal of Fluid Mechanics*, Vol. 658, Sept. 2010, pp. 509–538. doi:10.1017/S0022112010002375

[15] Bogey, C., and Bailly, C., "Influence of Nozzle-Exit Boundary-Layer Conditions on the Flow and Acoustic Field of Initially Laminar Jets," *Journal of Fluid Mechanics*, Vol. 663, Nov. 2010, pp. 507–538. doi:10.1017/S0022112010003605

[16] Bogey, C., Marsden, O., and Bailly, C., "Large-Eddy Simulation of the Flow and Acoustic Fields of a Reynolds Number 10^5 Subsonic Jet with Tripped Exit Boundary Layers," *Physics of Fluids*, Vol. 23, No. 3, 2011, Paper 035104.

[17] Bogey, C., Barré, S., and Bailly, C., "Direct Computation of the Noise Generated by Subsonic Jets Originating from a Straight Pipe Flow," *International Journal of Aeroacoustics*, Vol. 7, No. 1, 2008, pp. 1–22. doi:10.1260/147547208784079917

[18] Uzun, A., and Hussaini, Y., "Investigation of High Frequency Noise Generation in the Near-Nozzle Region of a Jet Using Large Eddy Simulation," *Theoretical and Computational Fluid Dynamics*, Vol. 21, 2007, pp. 291–321. doi:10.1007/s00162-007-0048-z

[19] Sandberg, R. D., Sandham, N. D., and Suponitsky, V., "DNS of Fully Turbulent Jet Flows in Flight Conditions Including a Canonical Nozzle," *17th AIAA/CEAS Aeroacoustics Conference and Exhibit*, AIAA Paper 2011-2918, June 2011.

[20] Sandberg, R. D., Sandham, N. D., and Suponitsky, V., "DNS of a Compressible Pipe Flow Exiting into a Coflow," *International Journal of Heat and Fluid Flow*, Vol. 35, 2012, pp. 33–44. doi:10.1016/j.ijheatfluidflow.2012.01.006

[21] Bogey, C., and Bailly, C., "Influence of Initial Turbulence Level on the Flow and Sound Field of a Subsonic Jet at a Diameter-Based Reynolds Number of 10^5," *Journal of Fluid Mechanics*, Vol. 701, 2012, pp. 352–385. doi:10.1017/jfm.2012.162

[22] Bühler, S., Obrist, D., and Kleiser, L., "Near-Field and Far-Field Acoustics of Laminar and Turbulent Nozzle Jet Flows," *19th AIAA/CEAS Aeroacoustics Conference and Exhibit*, AIAA Paper 2013-2195, May 2013.

[23] Müller, S., and Kleiser, L., "Large-Eddy Simulation of Vortex Breakdown in Compressible Swirling Jet Flow," *Computers & Fluids*, Vol. 37, 2007, pp. 844–856. doi:10.1016/j.compfluid.2007.04.010

[24] Müller, S., "Numerical Investigations of Compressible Turbulent Swirling Jet Flows," ETH Zurich, Rept. 17375, Zurich, 2007.

[25] Jarrin, N., Benhamadouche, S., Laurence, D., and Prosser, R., "A Synthetic-Eddy-Method for Generating Inflow Conditions for Large-Eddy Simulations," *International Journal of Heat and Fluid Flow*, Vol. 27, No. 4, March 2006, pp. 585–593. doi:10.1016/j.ijheatfluidflow.2006.02.006

[26] Jarrin, N., "Synthetic Inflow Boundary Conditions for the Numerical Simulation of Turbulence," Ph.D. Thesis, Univ. of Manchester, Manchester, England, U.K., 2008.

[27] Garnier, M. E., Adams, N., and Sagaut, P., *Large Eddy Simulation for Compressible Flows*, Springer, New York, 2009, pp. 179–184.

[28] Goldstein, M., "A Generalized Acoustic Analogy," *Journal of Fluid Mechanics*, Vol. 488, 2003, pp. 315–333. doi:10.1017/S0022112003004890

[29] Bogey, C., and Marsden, O., "Identification of the Effects of Nozzle-Exit Boundary-Layer Thickness and Its Corresponding Reynolds Number in Initially Highly Disturbed Subsonic Jets," *Physics of Fluids*, Vol. 25, No. 5, 2013, Paper 055106. doi:10.1063/1.4807071

[30] Bühler, S., "Direct Numerical Simulation of Laminar and Turbulent Nozzle-Jet Flows and Their Near-Field Sound," ETH Zurich ETH-21483, 2013.

[31] Tannehill, J. C., Anderson, D. A., and Pletcher, R. H., *Computational Fluid Mechanics and Heat Transfer*, 2nd ed., Taylor and Francis, Washington, D.C., 1997, pp. 338–341.

[32] Berland, J., Bogey, C., and Bailly, C., "Low-Dissipation and Low-Dispersion Fourth-Order Runge–Kutta Algorithm," *Computers & Fluids*, Vol. 35, 2006, pp. 1459–1463.

[33] Lele, S. K., "Compact Finite Difference Schemes with Spectral-Like Resolution," *Journal of Computational Physics*, Vol. 103, 1992, pp. 16–42. doi:10.1016/0021-9991(92)90324-R

[34] Frigo, M., and Johnson, S., "The Design and Implementation of FFTW3," *Proceedings of the IEEE*, Vol. 93, No. 2, 2005, pp. 216–231.

[35] Mohseni, K., and Colonius, T., "Numerical Treatment of Polar Coordinate Singularities," *Journal of Computational Physics*, Vol. 157, 2000, pp. 787–795. doi:10.1006/jcph.1999.6382

[36] Stolz, S., Adams, N. A., and Kleiser, L., "The Approximate Deconvolution Model for Large-Eddy Simulations of Compressible Flows and Its Application to Shock-Turbulent-Boundary-Layer Interaction," *Physics of Fluids*, Vol. 13, No. 10, 2001, pp. 2985–3001. doi:10.1063/1.1397277

[37] Tam, C. K. W., *Computational Aeroacoustics: A Wavenumber Approach*, 1st ed., Cambridge Univ. Press, New York, 2012, p. 379.

[38] Luginsland, T., Bühler, S., Obrist, D., and Kleiser, L., "A Parallel Code for Large Eddy Simulation of Compressible Swirling Jet Flows,"

Proceedings in Applied Mathematics and Mechanics, Vol. 10, No. 1, 2010, pp. 727–728.

[39] Bodony, D. J., "Aeroacoustic Prediction of Turbulent Free Shear Flows," Ph.D. Thesis, Stanford Univ., Stanford, CA, 2004.

[40] Spalart, P. R., "Direct Simulation of a Turbulent Boundary Layer up to $Re_\theta = 1410$," *Journal of Fluid Mechanics*, Vol. 187, 1988, pp. 61–98. doi:10.1017/S0022112088000345

[41] Colonius, T., "Modeling Artifical Boundary Conditions for Compressible Flow," *Annual Review of Fluid Mechanics*, Vol. 36, 2004, pp. 315–345. doi:10.1146/fluid.2005.36.01

[42] Thompson, K. W., "Time Dependent Boundary Conditions for Hyperbolic Systems," *Journal of Computational Physics*, Vol. 68, 1987, pp. 1–24. doi:10.1016/0021-9991(87)90041-6

[43] Kim, J. W., and Lee, D. J., "Generalized Characteristic Boundary Conditions for Computational Aeroacoustics, Part 2," *AIAA Journal*, Vol. 42, No. 1, 2004, pp. 47–55. doi:10.2514/1.9029

[44] Poinsot, T., and Lele, S., "Boundary Conditions for Direct Simulations of Compressible Viscous Flows," *Journal of Computational Physics*, Vol. 101, 1992, pp. 104–129. doi:10.1016/0021-9991(92)90046-2

[45] Schneider, W., "Flow Induced by Jets and Plumes," *Journal of Fluid Mechanics*, Vol. 108, 1981, pp. 55–65. doi:10.1017/S0022112081001985

[46] Touber, E., and Sandham, N. D., "Large-Eddy Simulation of Low-Frequency Unsteadiness in a Turbulent Shock-Induced Separation Bubble," *Theoretical and Computational Fluid Dynamics*, Vol. 23, 2009, pp. 79–107. doi:10.1007/s00162-009-0103-z

[47] Gräf, L., and Kleiser, L., "Large-Eddy Simulation of Double-Row Compound-Angle Film Cooling," *Computers and Fluids*, Vol. 43, No. 1, 2011, pp. 58–67. doi:10.1016/j.compfluid.2010.09.032

[48] Jarrin, N., Benhamadouche, S., Laurence, D., and Prosser, R., "A Synthetic-Eddy-Method for Generating Inflow Conditions for Large-Eddy Simulations," *International Journal of Heat and Fluid Flow*, Vol. 27, 2006, pp. 585–593. doi:10.1016/j.ijheatfluidflow.2006.02.006

[49] Smirnov, A., Shi, S., and Celik, I., "Random Flow Generation Technique for Large-Eddy Simulations and Particle-Dynamics Modeling," *Journal of Fluids Engineering*, Vol. 123, 2001, pp. 359–371. doi:10.1115/1.1369598

[50] Magagnato, F., Pritz, B., and Gabi, M., "Inflow Conditions for LES of Compressible Flow in a Combustion Chamber," *Proceedings of the 5th International Symposium on Turbulence, Heat and Mass Transfer*, edited by Hanjalic, Y. N. K., and Jakirlic, S., Dubrovnic, Croatia, 2006, pp. 343–346.

[51] Schlichting, H., *Grenzschicht-Theorie*, 5th ed., G. Braun, Karlsruhe, 1965, pp. 690–693.

[52] Colonius, T., and Lele, S., "Computational Aeroacoustics: Progress on Nonlinear Problems of Sound Generation," *Progress in Aerospace Sciences*, Vol. 40, 2004, pp. 345–416. doi:10.1016/j.paerosci.2004.09.001

[53] Jeong, J., and Hussain, F., "On the Identificatin of a Vortex," *Journal of Fluid Mechanics*, Vol. 285, 1995, pp. 69–94. doi:10.1017/S0022112095000462

[54] Wallace, J. M., Park, G., Wu, X., and Moin, P., "Boundary Layer Turbulence in Transitional and Developed States," *Physics of Fluids*, Vol. 24, No. 3, 2012, Paper 0035105.

[55] Pope, S. B., *Turbulent Flows*, 1st ed., Cambridge Univ. Press, Cambridge, England, U.K., 2000, pp. 324–327.

[56] Stewartson, K., "On the Flow Near the Trailing Edge of a Flat Plate," *Proceedings of the Royal Society of London*, Vol. 306, No. 1486, 1968, pp. 275–290.

[57] Harper-Bourne, M., "Jet Noise Measurements: Past and Present," *International Journal of Aeroacoustics*, Vol. 9, Nos. 4–5, 2010, pp. 559–588. doi:10.1260/1475-472X.9.4-5.559

[58] Hayes, M. H., *Statistical Digital Signal Processing and Modeling*, Wiley, New York, 1996, pp. 415–420.

[59] Lau, J. C., Morris, P. J., and Fisher, M. J., "Measurements in Subsonic and Supersonic Free Jets Using a Laser Velocimeter," *Journal of Fluid Mechanics*, Vol. 93, 1979, pp. 1–27. doi:10.1017/S0022112079001750

[60] Bogey, C., Marsden, O., and Bailly, C., "Effects of Moderate Reynolds Number on Subsonic Round Jets with Highly Disturbed Nozzle-Exit Boundary Layers," *Physics of Fluids*, Vol. 24, No. 10, 2012, Paper 105107. doi:10.1063/1.4757667

[61] Bogey, C., Barré, S., Fleury, V., Bailly, C., and Juvé, D., "Experimental Study of the Spectral Properties of Near-Field and Far-Field Jet Noise," *International Journal of Aeroacoustics*, Vol. 6, No. 2, 2007, pp. 73–92. doi:10.1260/147547207781041868

[62] Zaman, K. B. M. Q., "Far-Field Noise of a Subsonic Jet Under Controlled Excitation," *Journal of Fluid Mechanics*, Vol. 152, 1985, pp. 83–111. doi:10.1017/S0022112085000581

D. Gaitonde
Associate Editor